Large structures simulation for landscape evolution models

Julien Coatléven[1] and Benoit Chauveau[1]

[1]IFP Énergies nouvelles, 1 et 4 avenue de Bois-Préau, 92852 Rueil-Malmaison, France

Correspondence: Julien Coatléven (julien.coatleven@ifpen.fr)

Abstract. The aim of this paper is to discuss the efficiency of a new methodology to maintain the accuracy of numerical solutions obtained from our landscape evolution model (LEM). As in every LEM, the tricky part is the coupling between water and sediment flows that drives the non-linear self amplification mechanisms. But this coupling is also responsible for the emergence and amplification of numerical errors, as we illustrate here. These numerical instabilities being strongly reminiscent of turbulence-induced instabilities in computational fluid dynamics (CFD), we introduce a "large structures simulation" (LSS) approach for LEM, mimicking the large eddy simulations (LES) used for turbulent CFD. In practice, this treatment consists in a filtering strategy that controls small-scale perturbations in the solution. We demonstrate the accuracy of the LSS approach in the context of our LEM model.

1 Introduction

Since the pioneering work of Gilbert in the XIX century (Gilbert (1880)), the meaning of the term “landscape evolution model” (LEM) has evolved until reaching in the late XX century its modern definition. It is now considered has a numerical application of a mathematical system that seeks to simulate a part of the physical processes controlling the landscape dynamic. The capability of LEMs to provide an integrated simulation in which several processes are addressed make them particularly relevant to tackle a large variety of contexts. The success of those numerical approaches depends on their ability to correctly handle the positive non-linear feedback between the water flow, the sediment erosion and deposition in a decent computational time. This non-linear coupling between water and sediments is indeed expected to potentially induce complex water flow networks even on initially small topographic variations, allowing in return the emergence of complex geomorphic landforms. Some algorithms, in particular the family of MFD algorithms, have long been developed for solving surface water flow models in a low computational time. Until very recently, these solvers were not really linked to any physical model, which ruled out the use of an analytic solution to compare practical numerical results. It was therefore difficult to decipher if the obtained landform results only from physical processes or from the self-amplification of initially small numerical errors. An alternative definition of the specific catchment area often used to model water flow was proposed in Gallant and Hutchinson (2011); Bonetti et al. (2018), consisting in solving an abstract uniform flow equation in replacement of using one of the MFD algorithms. Independently and following an another path, in Coatléven (2020) a first MFD algorithms family (those for which water is transferred from cell to cell) has been proved to coincide on cartesian meshes with a classical discretization of the water mass conservation Gauckler-Manning-Strickler model (GMS). The output of the MFD algorithms is exactly a mesh-dependent mean of the water flux associated with the discrete GMS model. This result explains the mesh and numerical dependency since the output of the MFD does not fulfill the consistency criteria, but it also provides a way to correct it in a post-processing step leading to a consistent discrete approximation of the GMS water flux, extended in Coatléven (2020) to general polygonal meshes. As the GMS model can be seen as a generalization of the model proposed in Gallant and Hutchinson (2011); Bonetti et al. (2018), this finally closes the loop between MFD algorithms and the specific catchment area defined in Gallant and Hutchinson (2011); Bonetti et al. (2018) (more details are given in section 2.1). For those reasons, in the present paper we will use a general GMS model to compute our water flow.

This paper has two objectives: (1) to investigate the conditions for which the geomorphic structures simulated from of a landscape evolution model derive from numerical instabilities; (2) to introduce a methodology that improves the accuracy of the numerical solution and to discuss its potential importance for LEMs. The landscape evolution model used in this paper considers the GMS model for the surface water flow coupled with a representative erosion and deposition sediment flux model detailed in section (2.2), that has been previously used for instance in Granjeon (1996); Eymard et al. (2004, 2005); Peton et al. (2020) and which is a generalization of the models studied in Smith and Bretherton (1972); Smith et al. (1997). The linear stability analysis of this model brings out the key parameters that control the self-amplification mechanisms of the various water-sediment flow regimes (see section 2.3). To illustrate the related numerical issues, we test the convergence of numerical solutions towards some prescribed analytic solutions for various water-driven and gravity transport coefficients. Comparison between the analytic and numerical solutions leads us to the conclusion that numerical errors must be treated with the greatest care to avoid any misinterpretation of LEM results: the self-amplification processes at the core of the coupling between water flow and sediment evolution can amplify legitimate numerical round-off or solver errors. Thus estimating the relative impact of numerical errors on the final geomorphologic structures is challenging, making potentially hazardous the use of numerical approaches in particular those involving implicit time schemes to discuss and quantify the role of self-amplification mechanisms in realistic geodynamic contexts (e.g. the valley formation and spacing Scheingross et al. (2020); Bonetti et al. (2020); Perron et al. (2009); Hooshyar and Porporato (2021b)).

This self-amplification ("butterfly effect") is very reminiscent of the numerical issues arising in the field of computational fluid dynamics (CFD) for turbulent flows, which prevents the use of direct numerical simulation for high Reynolds numbers unless high order methods are used over small space and time scales (along with sometimes some blow up problems). This comparison with CFD and turbulent flows is not new and was studied in details for instance in Bonetti et al. (2020); Hooshyar et al. (2020). The modern solution found by the CFD community to achieve reproducible and meaningful simulations is to replace direct numerical simulation (DNS) of the Navier-Stokes equations by large eddy simulation (LES, Berselli et al. (2005)). The objective of LES is to obtain a good approximation of local spatial averages of turbulent flows, recovering the correct dynamics only for the organized structures of the flow (the eddies) which are larger than a certain α target length scale. Thus, LES chooses to abandon the idea of resolving all the scales involved in real physical processes, as there is no hope of using a mesh fine enough to resolve the smallest scales correctly. In practice this is done by filtering the solution to distinguish the flow behavior above and below α, and obtaining local averages that are smooth and as mesh independent as possible. To our knowledge, the first attempt at using a LES approach for simulating landscape evolution albeit without explicitly mentioning LES is Perron et al. (2009), where a Laplacian smoothing (equivalent to a mesh related box filter in the LES terminology) was applied to the topography. More recently Hooshyar and Porporato (2021a); Porporato (2022) have used an average in one direction (which is a limit case of filtering) to obtain robust results on channelization statistics and scaling signatures: in other words they substitute the elevation and the specific drainage area by their mean values in the axial direction of their rectangular simulated domain. In their conclusion they suggest that the use of LES approaches seems a viable avenue for more complex landscape evolution simulations. In line with this observation, we also believe that the success of the attempts of Perron et al. (2009); Hooshyar and Porporato (2021a); Porporato (2022), as well the numerous analogies between the instabilities arising in landscape evolution models and turbulence reported in Smith and Bretherton (1972); Scheingross et al. (2020); Bonetti et al. (2020); Hooshyar and Porporato (2021b) and the numerical experiments strongly advocate for the use of some LES technology to overcome the numerical issues arising in the non-linear coupling of sediment evolution and water flow. Our main contribution is precisely to develop a LES-type methodolgy for our LEM. We refer to this method by the acronym LSS for "large structures simulation". Notice that contrary to Hooshyar and Porporato (2021a); Porporato (2022) and more in line to what is done in the CFD community, we fix a length scale that corresponds to the size of the smallest structures we want to resolve in the problem, quite independently of the domain size. We also consider a more advanced differential filter, namely the Leray-α filter (Cheskidov et al. (2005); Guermond et al. (2003)) that is not related to any specific geometric configuration. In this sense, our work can be considered as a generalization of Hooshyar and Porporato (2021a); Porporato (2022). We show that when the filter size is correctly defined the results obtained from the LSS are actually free of the non-physical heterogeneity.

Obtaining a reproducible result and as error-free and mesh-independent as possible is, of course, what every modeler expects. On the other hand the emergence of complex geomorphologic structures, which is an objective sought by many LEM users, can require to manually introduce relevant physical heterogeneity after handling numerical errors. Several of our simulations are consequently performed using different types of heterogeneity carried by the initial topography or by other physical parameters, such as a a variable roughness index or a variable rain map. The emergence of large geomorphic structures is discussed by taking into consideration the understanding gained from this work.

The paper is organized as follows. We begin by introducing the water flow and the sediment flow models of the LEM used to perform the simulations discussed in this paper. We then construct analytic solutions and proceed to a comparison with numerical results in the relevant flow regimes. This leads to the first conclusion that for the studied landscape evolution model and the considered classical implicit finite volume discretization, without any specific treatment, the obtained numerical solutions are potentially controlled by numerical errors. The second step of this work is to introduce and apply the filtering strategy on the water-sediment equation system. The comparison between numerical and analytic solutions clearly shows the crucial role played by this method. Finally, we illustrate the behavior of our LEM in more complex contexts and we test the impact of variable (in space and time) roughness coefficients and rain maps in the final solution.

2 Model and notation

Following Smith and Bretherton (1972), we assume that a sedimentary system can be idealized through the following assumptions: (H1) the basin topography can be represented as a mathematical surface, (H2) the principle of the conservation of mass applies to this surface, (H3) the sediment flux at any point of the surface is a function of the local slope and the local discharge of water. In other words, using an Eulerian approach (H1) implies that we consider a fixed geographical region over the time period $]0,T[$ mathematically modeled by means of a domain $\Omega \in \mathbb{R}^2$, a function $b : \Omega \times]0,T[\longrightarrow \mathbb{R}$ describing the basement i.e. the lower part of the basin in the z direction, and a function $h_s : \Omega \times]0,T[\longrightarrow \mathbb{R}$ describing the thickness of the sediments (see Fig. 1). Thus, our basin $\mathcal{B} :]0,T[\longrightarrow \mathbb{R}^3$ can be described for almost every (a.e.) $t \in]0,T[$ by:

$$\mathcal{B}(t) = \left\{ (x,y,z) \in \mathbb{R}^3 \;\middle|\; (x,y) \in \Omega \text{ and } b(x,y,t) \leq z \leq b(x,y,t) + h_s(x,y,t) \right\}. \tag{1}$$

The evolution of the basement b is governed by several processes, for instance thermal and structural tectonics. In the present paper we assume that the evolution of b is a data, and we focus on computing the evolution of the function h_s. For the sake of clarity, we give the expression of the mass conservation (H2) equations, neglecting porosity for simplicity:

$$\left| \begin{array}{ll} \dfrac{\partial h_s}{\partial t} + div\,(\boldsymbol{J}_s) = S_s & \text{in } \Omega \times]t_0,T[, \\[2ex] -\boldsymbol{J}_s \cdot \boldsymbol{n} = B_s & \text{on } \partial\Omega_{\mathcal{N}} \times]t_0,T[, \\[2ex] h_s = 0 & \text{on } \partial\Omega_{\mathcal{D}} \times]t_0,T[, \\[2ex] h_s(t = t_0) = h_{s,0} & \text{in } \Omega, \end{array} \right. \tag{2}$$

where S_s and B_s are sediment source terms (coming from an in-situ sediment production, from soil erosion, or from sediment supplies defined in the domain boundaries) and $\boldsymbol{J}_s$ is the sediment flux. The domain boundary $\partial\Omega$ is divided between $\partial\Omega_{\mathcal{N}}$ where flux (also called Neumann) boundary conditions are imposed and $\partial\Omega_{\mathcal{D}}$ where we enforce fixed elevation (also called Dirichlet) boundary conditions. Let us precise that in the following the xy coordinates corresponding to the computational domain Ω will be expressed in kilometers (km), while sediment height h_s and basement b will be expressed in meters (m). Choosing a model corresponds to choosing a specific expression for the sediment flux and the source terms. A common feature of almost all LEMs is that the sediment flux model $\boldsymbol{J}_s$ and/or the source term S_s depend non-linearly on the local discharge of water $\mathcal{Q}_w$, very often through a power law like $\mathcal{Q}_w^{r_s} ||\nabla(h_s + b)||^{p_s+1}$. Self-amplification mechanisms are known to appear at least for $r_s > 1$ (Smith and Bretherton (1972); Smith et al. (1997)).

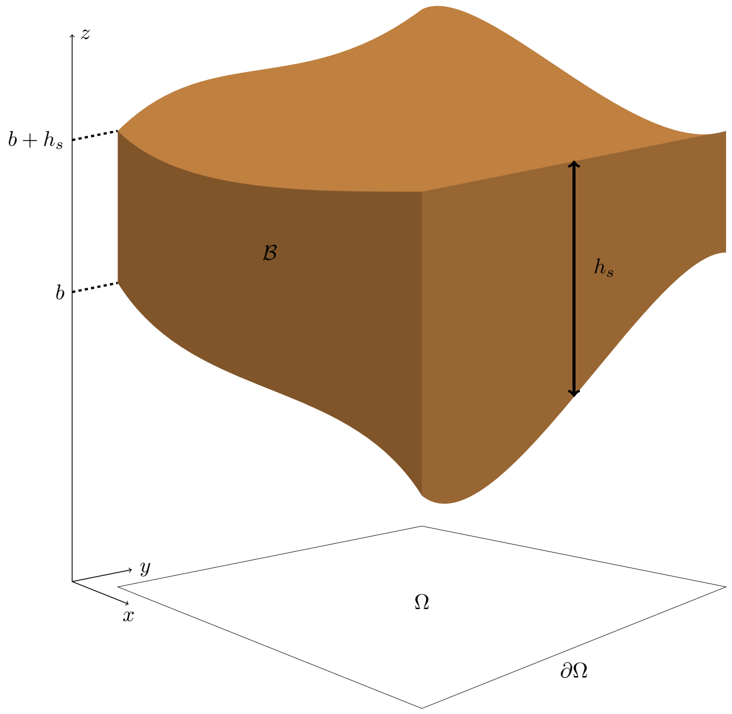

Figure 1. Representation of the two main surfaces considered in a landscape evolution model in the (x, y, z), parameter space, where z is the elevation and Ω the spatial domain for (x, y) with boundary $\partial\Omega$. The basement b surface represents the bottom part of the simulated block, on which sediments are deposited. The topographic surface is $b + h_s$ where h_s is the sediment thickness. The simulated sedimentary content is denoted $\mathcal{B}$.

2.1 The water flow model

Landscape evolution models usually defines the "local discharge of water" $\mathcal{Q}_w$ directly from the so-called drainage or catchment area CA (also referred as the contributing area). It corresponds at a given outlet to the measure of the horizontal projection of the surface area from which the water contributing to this outlet is coming from (Maxwell (1870); Leopold et al. (1964); Bonetti et al. (2018)). Despite being a very intuitive notion, it has evaded for a long time a precise mathematical definition. Classical multiple flow direction (MFD) algorithms are intended to provide a practical way at computing CA for a mesh cell. As is well documented (Desmet and Govers (1996); Pelletier (2010, 2013); Porporato (2022)) the discrete catchment area obtained from those algorithms strongly depends on the cell size, geometry and orientation with respect to the flow. Several attempts can be found in the literature to reduce this mesh dependency, defining the water flow discharge as $\mathcal{Q}_w = (CA/w)$, where w is a normalization factor related to a geometric property of the cell (cf Desmet and Govers (1996)) or to an estimate of the flow width (Pelletier (2010)) defining the so-called specific or unit catchment area (SCA/UCA). A more modern mathemat-

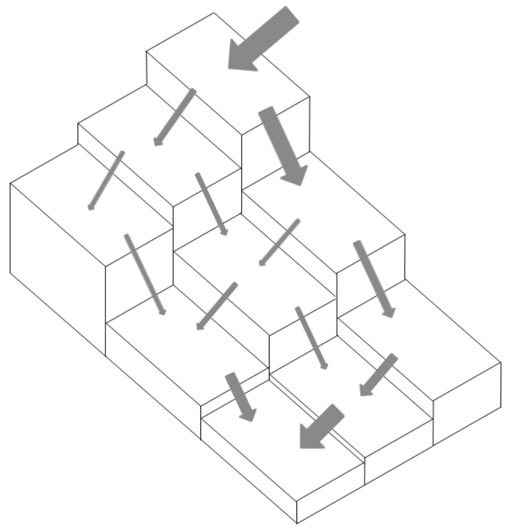

Figure 2. Basic principle of the simplest cell-to-cell MFD algorithm: water is distributed to lower neighboring cells proportionally to the slope (reproduced from Coatléven (2020))

ical definition of the specific catchment area a was proposed in Gallant and Hutchinson (2011); Bonetti et al. (2018), consisting in solving an abstract uniform flow equation:

$$\left|\begin{array}{ll} -div\left(a\dfrac{\nabla(h_s+b)}{||\nabla(h_s+b)||}\right)=1 & \text{in } \Omega, \\ -a\dfrac{\nabla(h_s+b)}{||\nabla(h_s+b)||}\cdot \boldsymbol{n}=0 & \text{on } \partial\Omega_{in}, \end{array}\right. \tag{3}$$

where $\partial\Omega_{in}=\{\boldsymbol{x}\in\partial\Omega \mid \nabla(h_s+b)\cdot\boldsymbol{n}>0\}$ is the part of the boundary that is in going and $\boldsymbol{n}$ denotes the outward normal to Ω. Setting $\mathcal{Q}_w=a$, this allows to reduce the mesh dependency to the usual consistency errors of numerical schemes.

At first sight, model (3) could seem very different from MFD algorithms. However, considering for instance the classical cell-to-cell algorithms of Freeman (1989, 1991); Holmgren (1994), one can see that those algorithms act as if one was distributing a fictitious water flow of a mesh cell to the neighboring cells with lower elevation proportionally to a function of the slope, as illustrated on figure 2. One could then legitimately assume that those MFD algorithms could be related to a discretization of some water flow model. This is precisely the idea of Coatléven (2020), where it was proved that the most classical cell-to-cell MFD algorithms are finally simply a way of implementing a solver for the following stationary water mass conservation with Gauckler-Manning-Strickler (GMS) flux modeling surface runoff:

$$\left|\begin{array}{ll} -div\left(k_m h_w \eta_w(h_w) s_{ref}^{-p_w}||\nabla(h_s+b)||^{p_w}\nabla(h_s+b)\right)=S_w & \text{in } \Omega, \\ -k_m h_w \eta_w(h_w) s_{ref}^{-p_w}||\nabla(h_s+b)||^{p_w}\nabla(h_s+b)\cdot n=0 & \text{on } \partial\Omega_{in}, \end{array}\right. \tag{4}$$

where h_w is the water height, s_{ref}= 1 m.km^{-1} the reference slope, p_w a model parameter and η_w the water mobility function. For simplicity we assume here that the mobility function has no dimension, and that the source S_w is given in m^3.s^{-1}km^{-2} such that its integral over a 2d area measured in km^2 coincides with a discharge in m^3.s^{-1}. The coefficient k_m can be though of as the Strickler coefficient or the inverse of the Gauckler-Manning coefficient up to a change of unit (strictly speaking, this identification is trully valid for channels and if the mobility function η_w is equal to a dimensionless hydraulic radius). For this choice of source, k_m has the unit m.s^{-1} of a speed. Comparing (4) with (3), we see that (3) corresponds to the particular case where $k_m = 1$, $p_w = -1$ and $a = h_w\eta_w(h_w)$. In this sense the GMS model (4) is a generalization of (3) that allows to include the classical ingredients (non linear slope dependency and some spatial heterogeneity) of the MFD algorithms family.

The analysis of Coatléven (2020) explains how the catchment area $CA(\mathcal{O})$ for the outlet of a region $\mathcal{O}$ that is computed by MFD algorithms coincides with an intermediate discrete quantity appearing in the most natural discrete solver for (4). It also allows to give a continuous interpretation of the $CA(\mathcal{O})$ that is computed by MFD algorithms:

$$CA(\mathcal{O}) = \int\limits_{\partial\mathcal{O}} h_w\eta_w(h_w)\left(-k_m s_{ref}^{-p_w}||\nabla(h_s+b)||^{p_w}\nabla(h_s+b)\cdot\boldsymbol{n}\right)^+, \tag{5}$$

where h_w is the solution of (4) with $S_w = 1$ and where we have denoted v^+ the positive part of v (i.e. $v^+ = max(0,v)$). Since model (4) describes a water flow, we recover that thanks to Coatléven (2020) we can reinterpret the catchment are $CA(\mathcal{O})$ computed through the classical cell-to-cell MFD algorithms the total flux leaving $\mathcal{O}$ of a fictitious water flow with a uniform water source $S_w = 1$. Unfortunately, we also see that $CA(\mathcal{O})$ strongly depends on the geometry of $\mathcal{O}$ and its orientation with respect to the flow. In particular, it is detailed in Coatléven (2020) that cell-to-cell MFD computations will compute in practice the catchment area $CA(\mathcal{K})$ for each cell K of a mesh through a discretized version of (5) for $\mathcal{O} = K$. Thus, when MFD algorithms are considering this expression of (5) to estimate the "local discharge of water" $\mathcal{Q}_w$, it produces cell and thus mesh dependency in the simulated surface water distribution. In line with the attempts of Desmet and Govers (1996) or Pelletier (2010) to define a specific catchment area (SCA) by rescaling the CA, the correct scaling would be to set the normalization factor w to the length of the portion of $\partial\mathcal{O}$ along which the fictitious water flow is leaving $\mathcal{O}$. A corrected definition of the specific catchment in the spirit of Desmet and Govers (1996); Pelletier (2010, 2013) area would thus be to use:

$$SCA(\mathcal{O}) = \frac{1}{\int\limits_{\partial\mathcal{O}} \chi_{-k_m s_{ref}^{-p_w}||\nabla(h_s+b)||^{p_w}\nabla(h_s+b)\cdot\boldsymbol{n}>0}} \int\limits_{\partial\mathcal{O}} h_w\eta_w(h_w)\left(-k_m s_{ref}^{-p_w}||\nabla(h_s+b)||^{p_w}\nabla(h_s+b)\cdot\boldsymbol{n}\right)^+, \tag{6}$$

where χ is the indicator function (i.e. the function with value 1 when the condition is satisfied and 0 otherwise). Depending on the orientation of the flow, such a normalization will sometimes match the choices of Desmet and Govers (1996) or Pelletier (2010, 2013) explaining their partial success. This SCA scales as an approximation of the continuous water flux magnitude:

$$q_w = |k_m h_w \eta_w(h_w)|\, s_{ref}^{-p_w}||\nabla(h_s+b)||^{p_w+1}, \tag{7}$$

(in m^{3}s^{-1}km^{-1}) but is not equal to it. The SCA defined by (6) is in fact a mean of q_w along the outflow portion of $\partial\mathcal{O}$, and thus still retains some dependency in the geometry of $\mathcal{O}$ and its orientation with respect to the flow. Meanwhile, notice that the specific catchment area a of model (3) can be reinterpreted through (4) as computing q_w since:

$$q_w = |k_m h_w \eta_w(h_w)|\, s_{ref}^{-p_w} ||\nabla(h_s+b)||^{p_w+1} = |a|\ ||\nabla(h_s+b)||^{-1+1} = a,$$

as we have set $a = h_w\eta_w(h_w) \geq 0$, $p_w = -1$, $k_m = 1$ and $s_{ref} = 1$ to merge (3) inside (4). Thus, in view of the success of Bonetti et al. (2018) and within the context of (4) it seems very natural to set $\mathcal{Q}_w = q_w$. One could consider that the equivalence between classical cell-to-cell MFD algorithms established in Coatléven (2020) and the consistency correction proposed there that leads to consider using a discrete version of q_w is another path to recover the conclusions of (3) and in this sense that q_w is a generalization of a to more complex water flow models.

The consistency correction proposed in Coatléven (2020) for MFD algorithms precisely coincides precisely with the replacement of the computation of $CA(K)$ or $SCA(K)$ for a mesh cell K by a consistent discrete reconstruction q_K of q_w in each cell K. Convergence of this discrete version q_K to q_w when the mesh size goes to zero was proved in Coatléven (2020), along with error estimates. Thus, apart from the usual discretization error no anomalous mesh dependency should remain in q_K in practice, contrary to what is observed for $SCA(K)$ given by MFD algorithms. In this sense, q_K can be seen as consistency correction for $SCA(K)$, as well as a generalization of (3) to a richer family of flow models. The interpretation of the local water discharge $\mathcal{Q}_w$ as being equal to the water flux magnitude q_w given by (7) from the solution of (4) is therefore the default configuration chosen in the water flow model used to perform all the simulations we introduce in this paper.

This water flow model is therefore physically justified by the GMS model. Its application domain is however not necessarily restricted to channels. It depends in fact to the specific choice made on the model parameter values. Steady state analysis (Graf and Altinakar (2000); Birnir et al. (2001)) for channels suggests to use values $\eta_w(h_w) = (h_w/h_{ref})^{1/2}$ and $p_w = -1/2$, while the classical Gauckler-Manning-Strickler formula would coincide with $\eta_w(h_w) = (R_h(h_w)/h_{ref})^{2/3}$ with $R_h(h_w)$ the hydraulic radius and again $p_w = -1/2$. When applied to large time and space scales landscape evolution models, these calibrations are no more valid and at this stage we suggest to consider η_w and p_w as modeling parameters that can be tuned for each considered problem. In the following numerical experiments, since we only consider the water fluw q_w the choice of the water mobility function as no influence and we set $\eta_w(h_w) = 1$ for simplicity, as well as $p_w = 0$. Notice that our conclusions would remain valid for more general choices of those parameters. The application domain is however limited by an additional mathematical condition. Notice that systems (3) and (4) are in fact stationary transport problems for a or h_w, which are rigorously speaking well-posed if the topography satisfies a sufficient condition. In particular conditions:

$$-\Delta\left(h_s+b\right) > 0 \quad \text{or} \quad -div\left(k_m s_{ref}^{-p_w} ||\nabla(h_s+b)||^{p_w} \nabla(h_s+b)\right) > 0, \tag{8}$$

ensures that model (4) is well-posed, which corresponds to prohibiting water accumulation areas and flat areas (see Coatléven (2020); Bardos (1970); Veiga (1987); DiPerna and Lions (1989); Fernández-Cara et al. (2002); Girault and Tartar (2010)). Model (4) being in fact a simplification of the shallow water equation (see section section 5.2), this limitation can be seen as the price to pay to simulate the water flow mass conservation with a very low computational expense. At the cost of a higher computational time alternative models also derived from the shallow water equation can be considered to overcome this limitation (see section 5.2).

2.2 The sediment flux model

In the present paper we have chosen to focus on the stratigraphic model that has already been discussed in detail in Granjeon (1996); Eymard et al. (2004, 2005); Peton et al. (2020), and which is a generalization of the models studied in Smith and Bretherton (1972); Smith et al. (1997). The corresponding sediment flux $\boldsymbol{J}_s$ takes the following form:

$$\boldsymbol{J}_s = -\eta_s(h_s) s_{ref}^{-p_s} ||\nabla(h_s+b)||^{p_s} \left(\left(\frac{q_w}{q_{ref}} \right)^{r_s} \nabla\psi_w(h_s+b) + \nabla\psi_g(h_s+b) \right) \quad \text{in } \Omega\times]t_0,T[, \tag{9}$$

where $r_s > 0$ and $p_s > 0$ are model parameters, q_w is the water flux obtained from (4), q_{ref} and s_{ref} are dimensional factors, and η_s is a dimensionless sediment mobility function such that:

$$0 \leq \eta_s(u) \leq 1 \quad \text{and} \quad \eta_s(0) = 0, \tag{10}$$

whose main role is to ensure that the sediment height h_s remains positive. In the following we use:

$$\eta_s(u) = \left| \begin{array}{ll} 1 - \dfrac{h_c}{u+h_c} & \text{if } u \geq 0, \\ 0 & \text{otherwise} \end{array} \right. \tag{11}$$

with h_c a parameter. The function with subscript w is intended to model the water driven processes, while the function with subscript g models gravity related processes. We consider here the most common form for functions ψ_w and ψ_g corresponding to:

$$\psi_w(u) = \int_0^u k_w(v)dv \quad \text{and} \quad \psi_g(u) = \int_0^u k_g(v)dv, \tag{12}$$

where k_w and k_g are diffusion coefficients such that:

$$0 \leq k_g^- \leq k_g(u) \leq k_g^+ < +\infty \quad \text{and} \quad 0 \leq k_w^- \leq k_w(u) \leq k_w^+ < +\infty, \tag{13}$$

in such a way that:

$$\nabla\psi_w(h_s+b) = k_w(h_s+b)\nabla(h_s+b) \quad \text{and} \quad \nabla\psi_g(h_s+b) = k_g(h_s+b)\nabla(h_s+b), \tag{14}$$

so that the sediment flux follows the topographic slope $\nabla(h_s+b)$.

This sediment flux model is implemented in our modeling platform ArcaDES, and all the simulations shown in the following sections are performed using the ArcaDES platform (although ArcaDES is mentioned for the first time in a scientific paper, it is used since 2015 in the stratigraphic numerical forward model DionisosFlow™ initially developed by Granjeon (1996)). Both soil erosion and sediment deposition are considered. As ArcaDES is tailored for large time and space scales simulations, this is the reason why we have chosen to express the xy coordinates in kilometers (km), time in million years (My), sediment height h_s and basement b in meters (m). Thus the unit of sediment sources will be meters per million years (m.My^{-1}). Since we have chosen to use $\mathcal{Q}_w = q_w$ with q_w the water flux from (4), the unit for the water discharge q_w is m^3.s^{-1}.km^{-1} and thus we naturally set q_{ref}= 1 m^3.s^{-1}.km^{-1}. The natural unit of coefficients k_g and k_w is km^2.My^{-1}, with the reference slope again set to s_{ref}= 1 m.km^{-1}.

2.3 Some insights from perturbation theory

In this subsection, in order to give a feeling of the potential stability issues related to model (2)-(9)-(4), we will perform a brief analysis of the behavior of solutions under perturbations. We assume for simplicity that k_g and k_w are constant functions. Let us denote $(h_{s,*}, h_{w,*})$ a reference solution of (2)-(9)-(4) with sources $(S_{s,*}, S_{w,*})$, whose stability is to be tested. We denote $(h_{s,\delta}, h_{w,\delta})$ a perturbation of magnitude δ of this reference solution with perturbed source $(S_{s,*} + S_{s,\delta}, S_{w,*} + S_{w,\delta})$ and consider the evolution of $(h_s, h_w) = (h_{s,*} + h_{s,\delta}, h_{w,*} + h_{w,\delta})$. Since both the perturbed and unperturbed solutions have to satisfy the boundary conditions, we deduce that the perturbation $(h_{s,\delta}, h_{w,\delta})$ itself also satisfies the same boundary conditions. Then in line with for instance the analysis of Smith et al. (1997), injecting (h_s, h_w) into (2)-(9), multiplying by $h_{s,\delta}$ and integrating by parts we get:

$$\frac{d}{dt}\left(\frac{1}{2}\int\limits_{\Omega} h_{s,\delta}^2\right) = -\int\limits_{\Omega} \eta_s(h_s) s_{ref}^{-p_s} ||\nabla(h_s+b)||^{p_s} \left(\left(\frac{q_w}{q_{ref}}\right)^{r_s} k_w + k_g\right) ||\nabla h_{s,\delta}||^2$$

$$+ \int\limits_{\Omega} \eta_s(h_{s,*}) s_{ref}^{-p_s} ||\nabla(h_{s,*}+b)||^{p_s} \left(\left(\frac{q_{w,*}}{q_{ref}}\right)^{r_s} k_w + k_g\right) \nabla(h_{s,*}+b)\cdot\nabla h_{s,\delta}$$

$$- \int\limits_{\Omega} \eta_s(h_s) s_{ref}^{-p_s} ||\nabla(h_s+b)||^{p_s} \left(\left(\frac{q_w}{q_{ref}}\right)^{r_s} k_w + k_g\right) \nabla(h_{s,*}+b)\cdot\nabla h_{s,\delta} + \int\limits_{\Omega} S_{s,\delta} h_{s,\delta}.$$

Denoting:

$$j_s(u,v,w) = \eta_s(u) s_{ref}^{-p_s} ||\nabla v||^{p_s} \left(\left(\frac{w}{q_{ref}}\right)^{r_s} k_w + k_g\right),$$

we obtain the equation governing the evolution of the perturbation's total energy:

$$\frac{d}{dt}\left(\frac{1}{2}\int\limits_{\Omega} h_{s,\delta}^2\right) = -\int\limits_{\Omega} j_s(h_s, h_s+b, q_w)||\nabla h_{s,\delta}||^2 + \int\limits_{\Omega} S_{s,\delta} h_{s,\delta}$$

$$+ \int\limits_{\Omega} \left(j_s(h_{s,*}, h_{s,*}+b, q_{w,*}) - j_s(h_s, h_s+b, q_w)\right)\nabla(h_{s,*}+b)\cdot\nabla h_{s,\delta}. \tag{15}$$

The first term of the right hand side is always negative and thus always contributes to the stability of the system. The second term describes the contribution to the evolution of the sediment perturbation's energy of potential pertubation sources other that the initial conditions. The last term:

$$A_\delta = \int\limits_{\Omega} \left(j_s(h_{s,*}, h_{s,*}+b, q_{w,*}) - j_s(h_s, h_s+b, q_w)\right)\nabla(h_{s,*}+b)\cdot\nabla h_{s,\delta}, \tag{16}$$

originates partially from the non-linearity of the sediment transport model but most importantly from the coupling between the flow and the sediment transport. If A_δ is negative or if it is small enough and if the perturbation source is also small enough, then the sediment perturbation energy will decrease with time. In this case, the solution $(h_{s,*}, h_{w,*})$ is said to be stable under perturbation $(h_{s,\delta}, h_{w,\delta})$. However the sign of A_δ is not always negative and will often take non necessarily small positive values. If A_δ is large enough, instead of being diffused by the first term the sediment perturbation energy will grow with time and potentially become as large as the unperturbed solution: the solution $(h_{s,*}, h_{w,*})$ is then unstable under perturbation $(h_{s,\delta}, h_{w,\delta})$. This is a self-amplification mechanism, as the magnitude of A_δ will grow with the perturbation's magnitude and cancel if the perturbation if zero, and also because of the dependency of the water flux $q_{w,\delta}$ on the topography perturbation $h_{s,\delta}$. We will say that growing perturbations correspond to the physically unstable regime.

We can anticipate that the relative magnitude of the gravity and water coefficients k_g and k_w will play a key role in the stability of solutions. Indeed denoting $\tau = (k_w q_w^{r_s})/(k_g q_{ref}^{r_s})$, if k_g is much larger than k_w large and thus τ is very small we have assuming for simplicity that $\eta_s = 1$:

$$A_\delta \approx k_g s_{ref}^{-p_s} \left(||\nabla(h_{s,*}+b)||^{p_s} - ||\nabla(h_s+b)||^{p_s}\right) \nabla(h_{s,*}+b)\cdot\nabla h_{s,\delta} + O(\tau)$$

$$\approx -k_g s_{ref}^{-p_s} \left(p_s ||\nabla(h_{s,*}+b)||^{p_s-2} |\nabla(h_{s,*}+b)\cdot\nabla h_{s,\delta}|^2\right) + O(\tau) + O(\delta^3).$$

(where we recall that a function f is $O(h)$ if there exists a constant $C>0$ independent on h such that $||f|| \leq Ch$ for a suitable norm $||.||$). Then for large values of k_g the term A_δ is always negative and thus stabilizing. On the contrary, if k_w is much larger than k_g then τ is also very large and we have:

$$A_\delta \approx -k_w s_{ref}^{-p_s} q_{ref}^{-r_s} \left(q_{w,*}^{r_s} ||\nabla(h_{s,*}+b)||^{p_s} - q_w^{r_s} ||\nabla(h_s+b)||^{p_s}\right) \nabla(h_{s,*}+b)\cdot\nabla h_{s,\delta} + O(1/\tau)$$

$$\approx -k_w s_{ref}^{-p_s} r_s \frac{q_{w,*}^{r_s-1}}{q_{ref}^{r_s}} q_{w,\delta} ||\nabla(h_{s,*}+b)||^{p_s} \nabla(h_{s,*}+b)\cdot\nabla h_{s,\delta}$$

$$-k_w s_{ref}^{-p_s} \left(\frac{q_{w,*}}{q_{ref}}\right)^{r_s} \left(p_s ||\nabla(h_{s,*}+b)||^{p_s-2} |\nabla(h_{s,*}+b)\cdot\nabla h_{s,\delta}|^2\right) + O(1/\tau) + O(\delta^3).$$

Regions for which $\nabla(h_{s,*}+b)\cdot\nabla h_{s,\delta} < 0$ will amplify the perturbation proportionally to k_w and the power $r_s - 1$ of the water flux. We also see that the term A_δ will behave quite differently if $r_s > 1$ or $r_s < 1$. Indeed, for $r_s > 1$ the water flux will reinforce the amplification term in a kind of positive feedback loop. On the contrary, for $r_s < 1$ the water flux will temper the amplification term, thus we can anticipate that it will require much larger values of τ for instability to occur in this situation. Going back to the general case for η_s, we have for small values of τ:

$$A_\delta \approx -k_g s_{ref}^{-p_s} \Big(\eta_s'(h_{s,*}) ||\nabla(h_{s,*}+b)||^{p_s} h_{s,\delta} \nabla(h_{s,*}+b)\cdot\nabla h_{s,\delta} +$$

$$p_s \eta_s(h_{s,*}) ||\nabla(h_{s,*}+b)||^{p_s-2} |\nabla(h_{s,*}+b)\cdot\nabla h_{s,\delta}|^2\Big) + O(\tau) + O(\delta^3).$$

while for large values of τ we have:

$$A_\delta \approx -k_w s_{ref}^{-p_s} r_s \frac{q_{w,*}^{r_s-1}}{q_{ref}^{r_s}} q_{w,\delta} \eta_s(h_{s,*}) ||\nabla(h_{s,*}+b)||^{p_s} \nabla(h_{s,*}+b)\cdot\nabla h_{s,\delta}$$

$$-k_w s_{ref}^{-p_s} \left(\frac{q_{w,*}}{q_{ref}}\right)^{r_s} \Big(\eta_s'(h_{s,*}) ||\nabla(h_{s,*}+b)||^{p_s} h_{s,\delta} \nabla(h_{s,*}+b)\cdot\nabla h_{s,\delta} +$$

$p_s\eta_s(h_{s,*})||\nabla(h_{s,*}+b)||^{p_s-2}|\nabla(h_{s,*}+b)\cdot\nabla h_{s,\delta}|^2\big)+O(1/\tau)+O(\delta^3).$

The behavior is roughly speaking the same, with the main difference that the additional term in $\eta_s^{'}(h_{s,*})$ can also contribute with the wrong sign. Since $\eta_s^{'}(h_{s,*})$ will be almost zero as soon as $h_{s,*}$ is large enough (see equation (11)), this can only happens in regions where $h_{s,*}$ is close to zero (in particular near Dirichlet boundaries). In this case, the potential contribution to the instabilities is controlled by the magnitude of $|\eta_s^{'}(h_{s,*})h_{s,\delta}|\leq|h_{s,\delta}|/h_c$. If the perturbation is not amplified by other engines, which will be the case if τ is small, and if the parameter h_c is not chosen too small (a typical valid value is 20 cm), then no severe instability can occur through this additional term. Thus we can be confident that parameter τ will be the main criterion governing the appearance of instabilities even for our most general model.

For a subclass of model (2)-(9)-(4) with $\eta_s=1$, $k_g=0$ and $p_w=-1$ and $p_s=0$, the stability of solutions have been theoretically studied in Smith and Bretherton (1972); Smith et al. (1997). It was for instance established in Smith et al. (1997) that if the reference solution is stationary, that the second term is negative only if some specific condition on the gradient $\nabla(h_s+b)$ is satisfied on the boundary of the region of interest, here Ω. The linear stability of analytic stationary solutions that are uniform in one direction has also been considered in Smith et al. (1997). Their conclusion is that under periodic perturbations in the transverse direction, for $r_s\leq 1$, the linear stability analysis does not reveal any instability while for $r_s>1$, the stationary solutions are linearly unstable if the frequency of the periodic perturbation is large enough. Notice that the case $p_w=-1$ greatly simplifies such studies: the linear stability analysis can be showed to be equivalent to solving a one dimensional ordinary differential equation.

The studies mentioned above are focused on the stability of physically meaningful solutions. Here, we want to draw attention on the numerical consequences of this self-amplification phenomenon, in this way we focus on the stability of numerical solutions. Let us explain the key idea: assuming that all functions are regular enough, one could consider (for instance in a finite difference setting) that our numerical solution is roughly speaking a perturbation of the exact continuous solution, where the source terms $S_{s,\delta}$ and $S_{w,\delta}$ represent the unavoidable consistency and solver errors of our solving process. Then the numerical sediment perturbation energy will satisfy (15) and will self-amplify in the same way than physical perturbations self-amplify. In the unstable regime, this means than the numerical solution can potentially diverge from the exact one from a large amount up to the point that it cannot be considered a relevant approximation of the continuous solution, even if the numerical perturbation arises from initially small numerical errors.

3 Numerical instabilities arising from the non linear coupling of overland flow and sediment dynamic

To illustrate the numerical issues linked to the self-amplification of initially small numerical errors, we consider in this section several situations where we have either the full knowledge of the exact solution or a criterion to distinguish it from incorrect solutions. Thanks to those information on the exact solution, we can illustrate the stability issues of simulations using model (2)-(9)-(4) (discretized by the finite volume scheme detailed in appendix C).

3.1 Instabilities for analytic solutions

In this subsection we consider stationary analytic functions of the form:

$$\left| \begin{array}{l} h_s^{ex}(x,y) = h_{s,x}(x) + \displaystyle\sum_{p=1}^{N_b} g_b\left(\frac{x-x_p}{\delta_x}, \frac{y-y_p}{\delta_y}\right), \\ h_w^{ex}(x,y) = h_{w,x}(x), \end{array} \right.$$

incorporating N_b small smooth bumps randomly positioned at points (x_p, y_p) chosen such that they do interfere with the boundary conditions, with the smooth bump function given by:

$$g_b(x,y) = g_b(r^2) = \left| \begin{array}{ll} H_{pert} \exp\left(\dfrac{-\gamma}{1-r^2}\right)\exp(\gamma) & \text{for } r^2 = x^2+y^2 \leq 1, \\ 0 & \text{otherwise .} \end{array} \right.$$

with in practice N_b=5, H_{pert}=0.03 m, γ=10 and δ_x=δ_y=0.25 km. The numerical domain is rectangular and centered at $(0,0)$ with the dimensions $Lx = 1$ km in the x axis and $Ly = 5$ km in the y axis, and the basement b is set to zero. We impose homogeneous Dirichlet boundary conditions ($h_s = 0$) on the boundaries $x = -Lx/2$ and $x = Lx/2$ and homogeneous Neumann boundary conditions ($\partial_y h_s = 0$) on the boundaries $y = -Ly/2$ and $y = Ly/2$ as illustrated on figure 3. We use for the

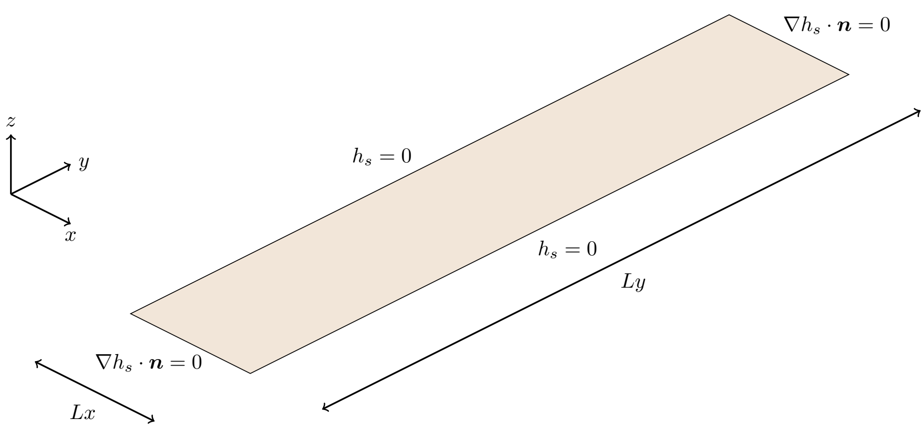

Figure 3. Domain configuration for the analytic tests cases

monodimensional functions $(h_{s,x}, h_{w,x})$ the stationary solution of model (2)-(9)-(4) in the case $\eta_s = 1$ given in appendix A that satisfies the boundary conditions. For all our simulations, the constant source terms ($S_{s,x}$,$S_{w,x}$) for the analytic the stationary solution $(h_{s,x}, h_{w,x})$ in the case $\eta_s = 1$ (see appendix A for details) are always equal to (10 m.My^{-1},1 m^3.s^{-1}km^{-2}). Injecting (h_s, h_w) into (2)-(9)-(4), after some straightforward but tedious computations one can derive exact expressions for the corresponding source terms (S_s^{ex}, S_w^{ex}), making the pair (h_s, h_w) an analytic solution of our model for those source terms.

Given those analytic source terms, initializing the sediment height to the analytic value $h_s(x,y,0) = h_s^{ex}(x,y)$ and the water height to the analytic value $h_w(x,y,0) = h_w^{ex}(x,y)$ the exact solution of model (2)-(9)-(4) is of course simply equal to (h_s^{ex}, h_w^{ex}) for all times. Thus, any reasonable numerical solution should remain a correct approximation of (h_s^{ex}, h_w^{ex}) for all times.

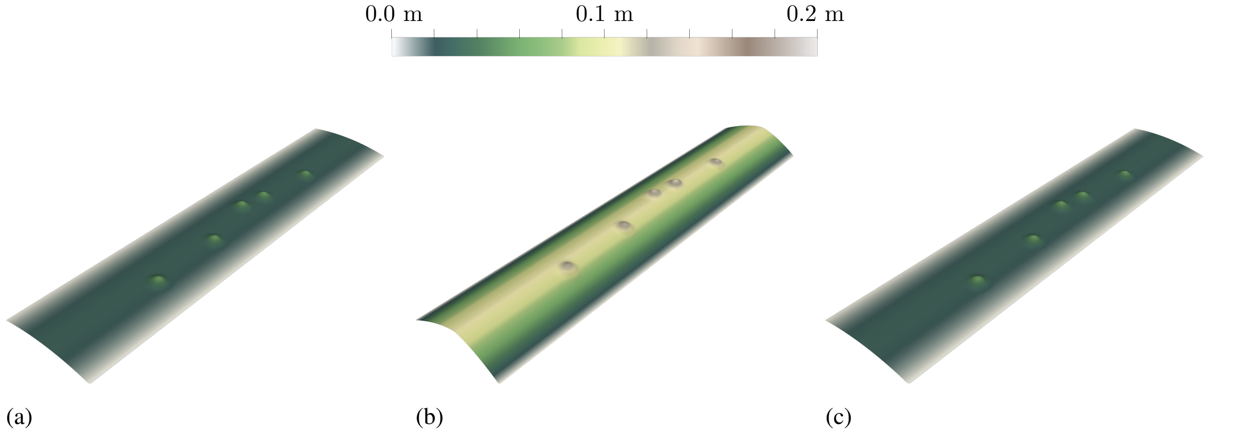

Figure 4. Sediment height h_s^{ex} of the analytic solution for the case k_g=50 km^2.My^{-1} and k_w=1 km^2.My^{-1}. a: r_s=1, p_s=0, b: r_s=3/2, p_s=1, c: r_s=2, p_s=0

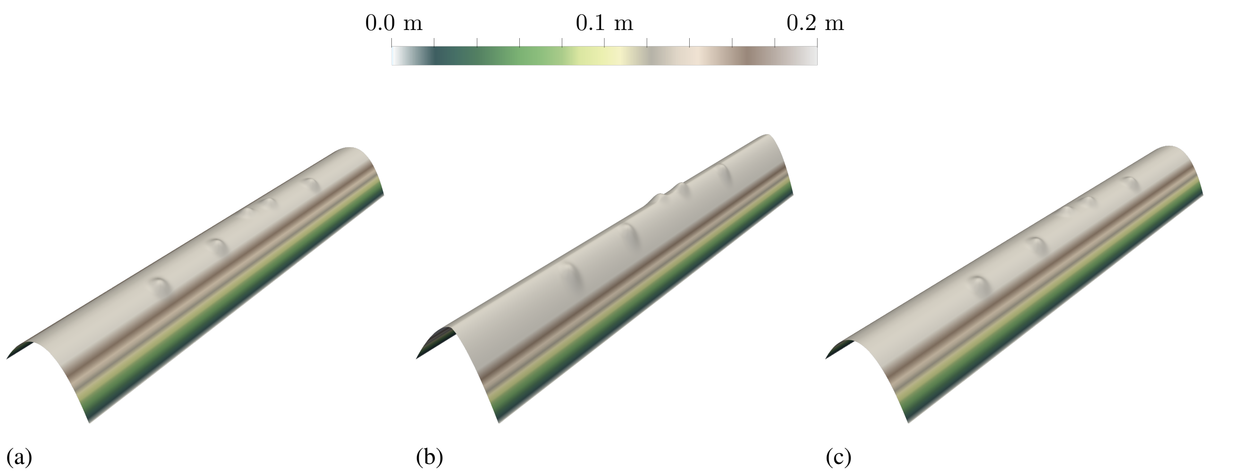

Figure 5. Sediment height h_s^{ex} of the analytic solution for the case k_g=5 km^2.My^{-1} and k_w=1 km^2.My^{-1}. a: r_s=1, p_s=0, b: r_s=3/2, p_s=1, c: r_s=2, p_s=0

Using the finite volume discretization described in appendix C on a cartesian mesh with square cells for which we denote Δ_{xy} the size of the edges of the cartesian cells, we attempt to reproduce the stationary analytic solution by initializing the

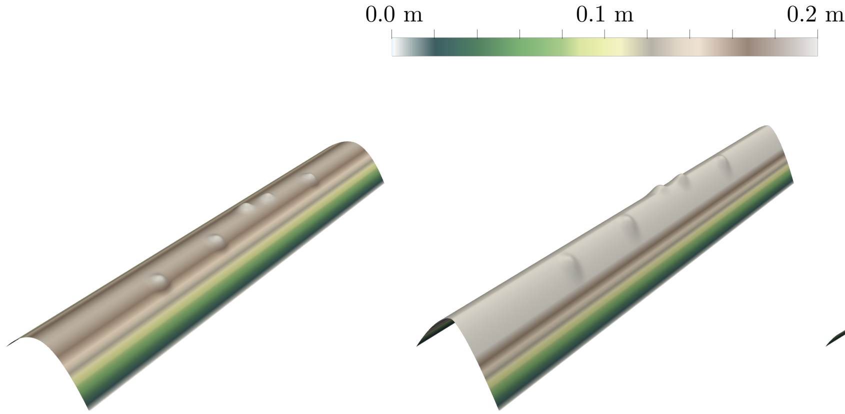

(a) (b) (c)

Figure 6. Sediment height h_s^{ex} of the analytic solution for the case k_g=5 km^2.My^{-1} and k_w=5 km^2.My^{-1}. a: r_s=1, p_s=0, b: r_s=3/2, p_s=1, c: r_s=2, p_s=0

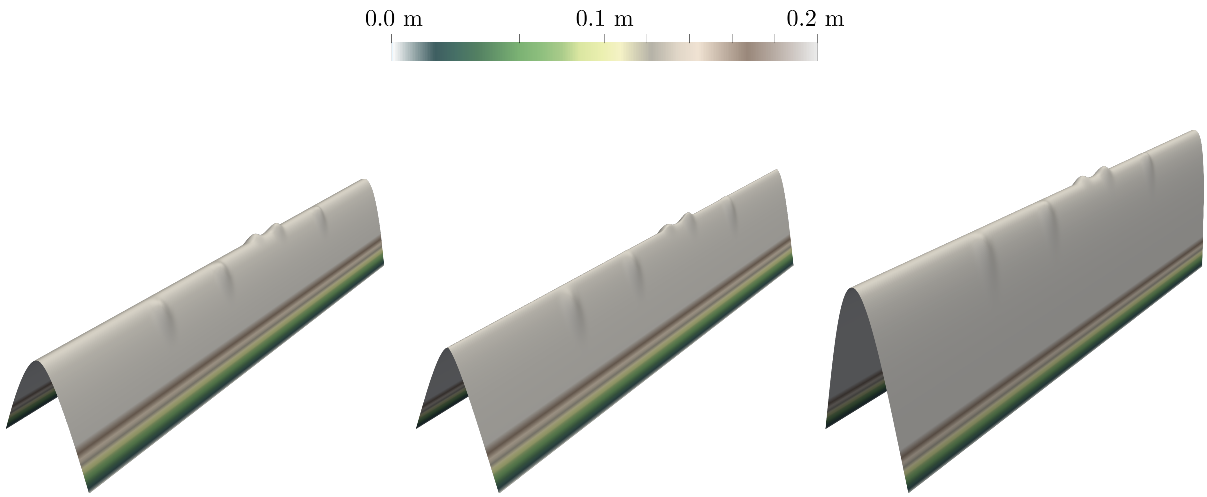

(a) (b) (c)

Figure 7. Sediment height h_s^{ex} of the analytic solution for the case k_g=1 km^2.My^{-1} and k_w=5 km^2.My^{-1}. a: r_s=1, p_s=0, b: r_s=3/2, p_s=1, c: r_s=2, p_s=0

system to $(h_s(x,y,0),h_w(x,y,0))$=$(h_s^{ex}(x,y),h_w^{ex}(x,y))$ and using the analytic source terms (S_s^{ex},S_w^{ex}), for various values of the parameters k_g, k_w r_s and p_s. The simulation total time is 0.25 My, and we use time steps of maximum length Δt=0.002 My. The corresponding analytic solutions are presented on figures 4, 5, 6 and 7 for the different values of the parameters k_g, k_w r_s and p_s we have considered. All those simulations have been performed in parallel on 108 processors through the use of

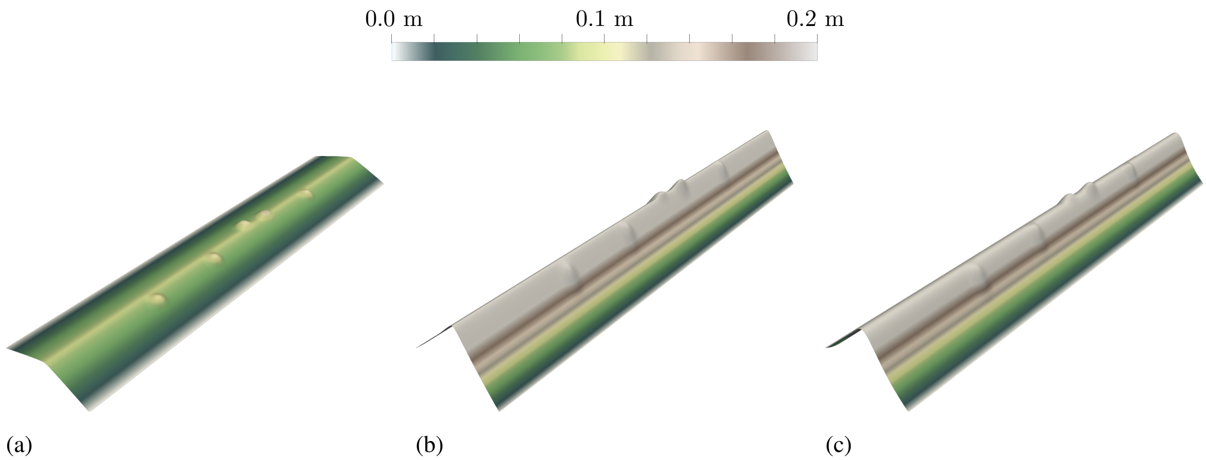

Figure 8. Sediment height h_s^{ex} of the analytic solution for the case k_g=1 km^2.My^{-1} and k_w=50 km^2.My^{-1}. a: r_s=1, p_s=0, b: r_s=3/2, p_s=1, c: r_s=2, p_s=0

Table 1. Approximate maximum analytic value of $\tau = \frac{k_w}{k_g}\left(\frac{q_w}{q_{ref}}\right)^{r_s}$ for each convergence test

	(r_s=1,p_s=0)	(r_s=3/2,p_s=1)	(r_s=2,p_s=0)
(k_g,k_w)=(50,1) km^2.My^{-1}	0.01	0.00353	0.0025
(k_g,k_w)=(5,1) km^2.My^{-1}	0.1	0.0353	0.025
(k_g,k_w)=(5,5) km^2.My^{-1}	0.5	0.353	0.25
(k_g,k_w)=(1,5) km^2.My^{-1}	2.5	1.767	1.25
(k_g,k_w)=(1,50) km^2.My^{-1}	25	17.67	12.5

the MPI library.

On figure 9, we present the obtained convergence curves for all the tested analytic solutions, i.e. we plot the standard L^2 error measuring the difference between the simulated sediment height and the exact analytic sediment height. We see on figure 9 that for all configurations except the case (k_g=1 km^2.My^{-1}, k_w= 50 km^2.My^{-1}), we obtain clean convergences curves, assessing the correctness of our numerical scheme even for the non-linear couplings. However, for the case (k_g=1 km^2.My^{-1}, k_w= 50 km^2.My^{-1}) the two non-linear couplings (r_s=3/2,p_s=1) and (r_s=2,p_s=0) fail to converge. Looking at table 1 where we regroup the value of τ for each test case using the knowledge of the exact solution, we see that convergence problems appear as expected when τ becomes large. Indeed, since the error increases when we refine the mesh, this error is not a discretization consistency error as moreover all the other test cases validate both our implementation and discretization. On the contrary it increases with the size of the numerical systems, which strongly suggests that it originates from solver (both linear and non-linear) errors, and this perfectly illustrates the phenomenon of numerical errors self-amplification that we have discussed from the theoretical

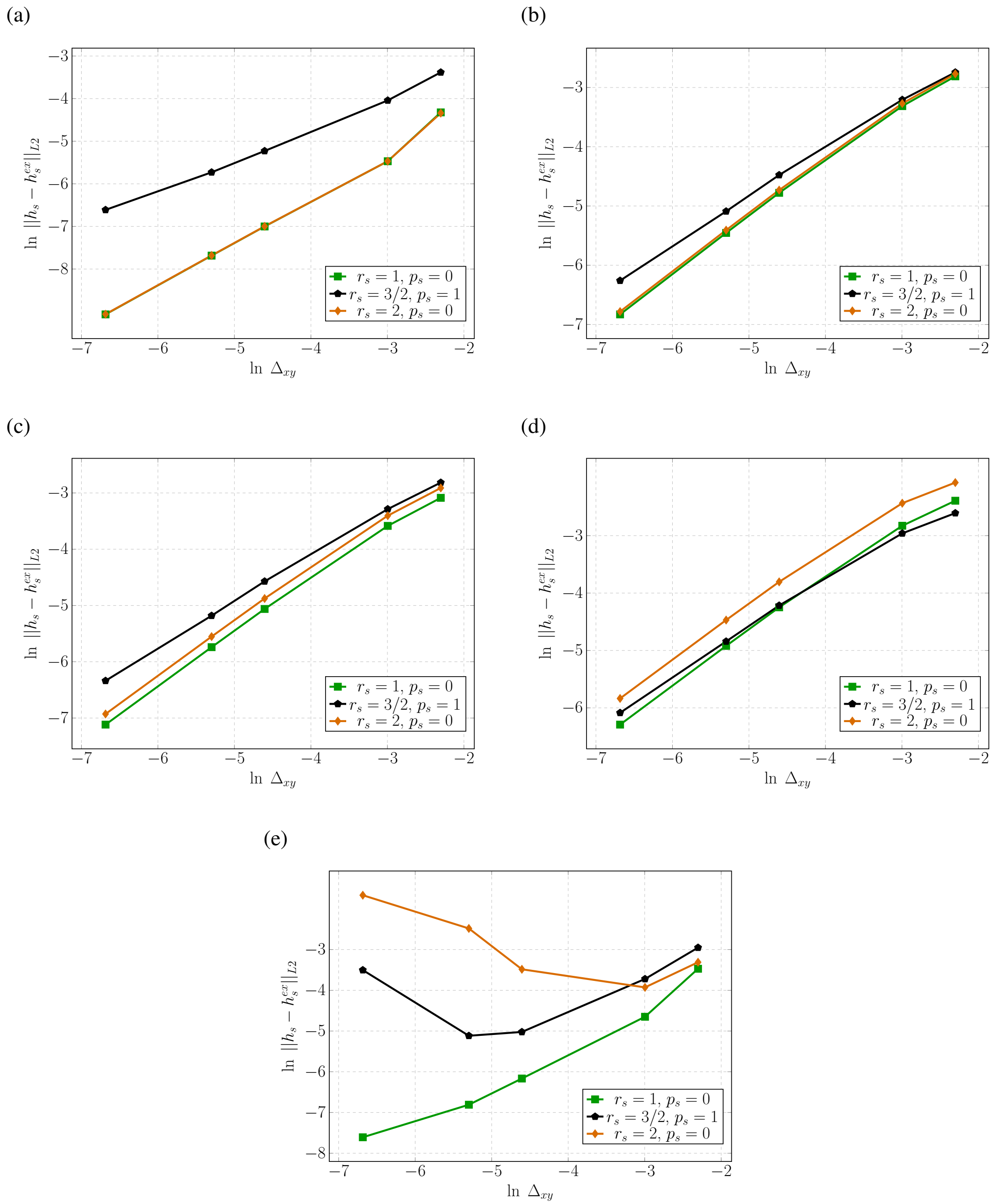

Figure 9. Convergence curves. a: case k_g=50 km^2.My^{-1} and k_w=1 km^2.My^{-1}. b: case k_g=5 km^2.My^{-1} and k_w=1 km^2.My^{-1}. c: case k_g=5 km^2.My^{-1} and k_w=5 km^2.My^{-1}. d: case k_g=1 km^2.My^{-1} and k_w=5 km^2.My^{-1}. e: case k_g=1 km^2.My^{-1} and k_w=50 km^2.My^{-1}

point of view in the section 2.3. Another reason for which problems are probably more severe with finer meshes is that numerical diffusion which is much smaller than the true physical diffusion in view of the values of k_g adds nevertheless enough additional smoothing for large values of Δ_{xy} to dissipate large parts of the numerical errors while this is no longer the case for the finer meshes.

Now, to illustrate how treacherous those numerical solutions are, we present on figures 10 and 11 a comparison between the analytic solution and its erroneous numerical counterpart.

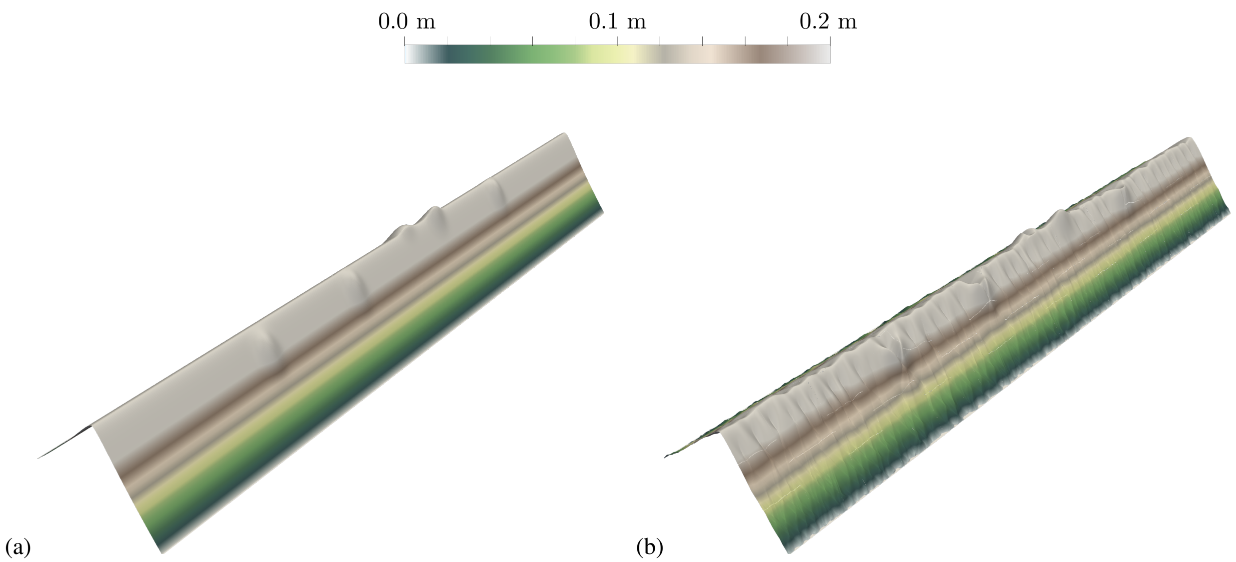

Figure 10. Comparion between the sediment height h_s^{ex} of the analytic solution and numerical solution h_s for the case k_g=1 km^2.My^{-1}, k_w=50 km^2.My^{-1}, $r_s = 3/2$ and p_s=1. a: Analytic solution h_s^{ex}, b: numerical solution h_s

The erroneous solutions are dangerously "good looking": indeed, if only the initial topography and the rain and production data are shown, one could easily be tempted to interpret the quite complex topographies obtained as the realistic self-amplification of the perturbations due to the presence of the bumps. However since we know the exact solution, we are sure that this is not the case: the appealing numerical solutions are completely wrong. The overall "geologically realistic" look of the erroneous solution comes from the fact that numerical noise is amplified not by some numerical scheme deficiency but by the capacity of our continuous model to amplify perturbations that we described in the previous section. In other words, the numerical noise is reworked by the system, giving a "realistic" look to it. This is the reason why we stress that when performing real-life simulations for which of course the correct solution is unknown (otherwise we would not need to simulate anything at all), it can become very hard to decide if the numerical results are correct or blurred by realistic looking amplified numerical noise. The quality of the numerical scheme, although essential, is not in question: the issue is the self-amplification mechanisms of

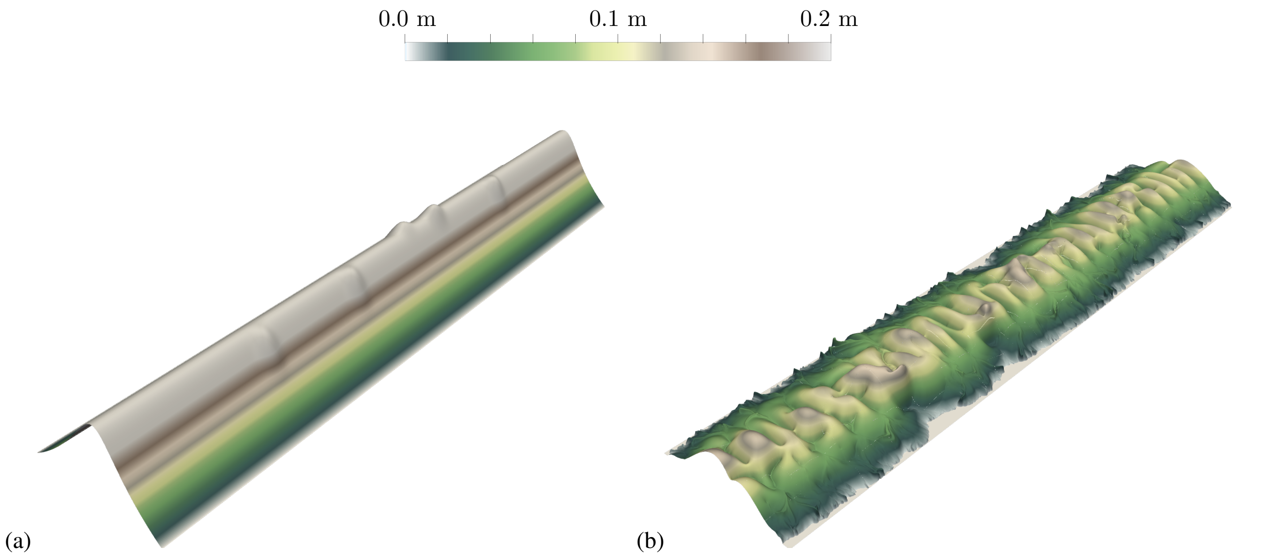

Figure 11. Comparion between the sediment height h_s^{ex} of the analytic solution and numerical solution h_s for the case k_g=1 km^2.My^{-1}, k_w=50 km^2.My^{-1}, $r_s = 2$ and p_s=0. a: Analytic solution h_s^{ex}, b: numerical solution h_s

the continuous model. They are the reason for its physical interest but simultaneously its main issue for performing reliable simulations.

3.2 Identifiable instabilities in a non analytic case

As mentioned in the introduction and above, in real applications one does not have a reference analytic solution and it is in general hard on complex topographies to decide whether a numerical solution of (2) is correct or not. To illustrate how one can sometimes partially circumvent this difficulty, we consider a simple synthetic topographic surface defined by three constant slope planes. The numerical domain is rectangular with the dimensions $Lx = 400$ km in the x axis and $Ly = 300$ km in the y axis (see Fig. 12-a,12-b). We use again a cartesian mesh with square cells, the edges of each cell being of length $\Delta_{xy} = 2$ km. The gravity diffusion coefficient k_g is equal to 100 km^2.My^{-1} in the whole domain while $k_w = 10$ km^2.My^{-1} for $h_s + b \geq 0$ and $k_w = 0.1$ km^2.My^{-1} for $h_s + b < 0$, corresponding to a modulation of the water induced transport in a fictitious marine domain. Water is supplied by three constant water-flux sources located at the domain boundary (black arrows in Fig. 12-a), so we call this “three rivers” test case. Each water source is 12 km large and supplies 1200 m^{3}s^{-1} of water.

An essential remark is that the whole configuration is symmetric with respect to the vertical plane $x = Lx/2$, including the cartesian mesh used for this simulation. In principle, the equation system consisting of (2) and (4), here used with $r_s = 2$, $p_s = 1$, should maintain this symmetry. Since we do not know this time the exact solution, at least we can use symmetry to identify erroneous results that do not fulfill this elementary requirement. Using the finite volume scheme depicted in section C, we perform a set of three identical simulations in terms of physical parameters but using different numerical settings in

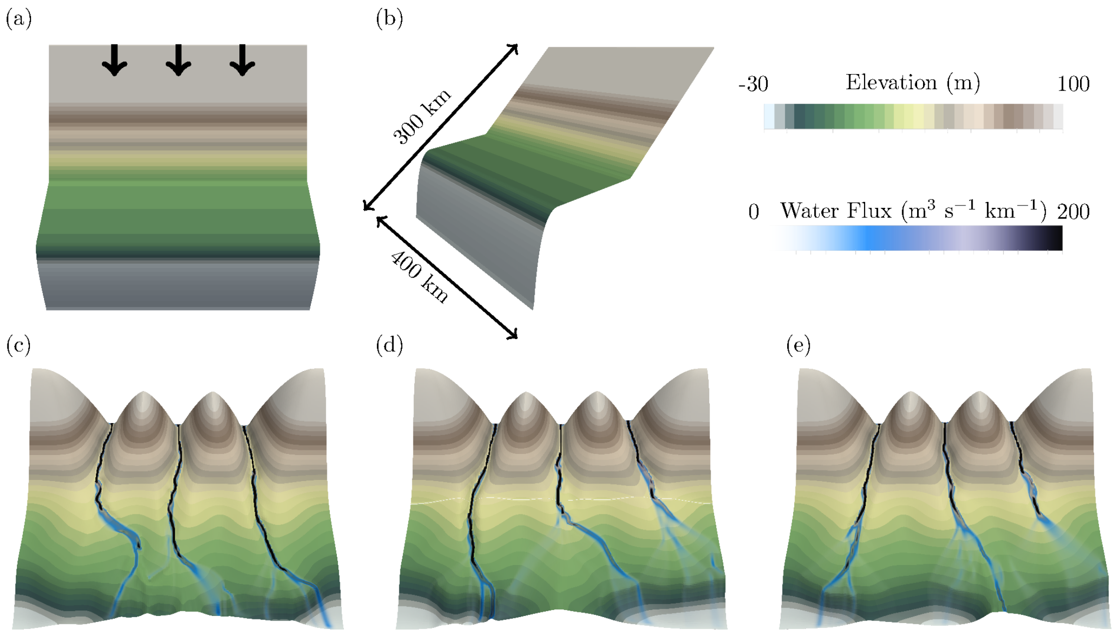

Figure 12. The "three rivers" test case with Δ_{xy}=2 km. a-b : Initial topography, black arrows represent the position of the water inflows. Bottom row : topography and water flux after 6 My obtained under different numerical settings. c: sequential GMRES, d: parallel GMRES, e: sequential BiCGStab

order to illustrate the impacts of numerical errors. For simplicity, the cartesian mesh shares the symmetry of the problem, to avoid any additional symmetry approximation error. We perform a sequential computation using GMRES as linear solver for all systems, its parallel equivalent on 4 processors and another sequential simulation using BiCGStab as linear solver for all systems. The linear solvers are part of the well-known and reference PETSc library (Balay et al. (1998)) to avoid any potential mistake in their implementation, while the parallelism relies on the Arcane framework (Grospellier and Lelandais (2009)). Final topographies and water flux are shown on the bottom row of Fig. 12. Figure 12-c corresponds to sequential GMRES, Fig. 12-d to parallel GMRES and Fig. 12-e to sequential BiCGStab.

All the results from these simulations should be almost identical and in any case symmetrical with respect to the vertical plane $x = Lx/2$ in absence of any spatial heterogeneity in the input data. Clearly, symmetry is lost in the three cases and what is even more striking is that we get three very different results. The only difference between the three cases being the numerical solvers, this indicates that this has originated from numerical errors. As we are using a decoupled time scheme between water flow and sediment evolution (see section C), one may argue that those instabilities are arising from some violated coupling constraint on the time step. Should this be the case, reducing the time step enough would ultimately lead to clean solutions. However, we have observed the exact opposite: the smaller the time step is, the larger are the obtained instabilities. The fact that reducing the time step makes things even worse is thus another clear sign that our problems are the result of amplified error accumulation up to the point that it influences flow branching.

4 Large structures simulation (LSS): an attempt to get rid of instabilities in LEMs

In this section, we explain how to transpose the ideas underlying the concept of large eddy simulation from the computational fluid dynamics community to our landscape evolution model. In our opinion, this is a key ingredient for achieving reproducible LEM simulations.

4.1 Principles and physical interpretation of filtering

Recall that the main idea of LES is to filter the solution to distinguish between the behavior of the flow above and below the target length scale, to obtain local averages that are smoother and as mesh independent as possible. This target length scale controls the size of the smallest structures that we will be able to resolve in the problem, quite independently of the domain size. The main practical consequence is that our mesh will have to resolve this length scale, i.e. the mesh size ε will have to be smaller than the chosen length scale.

LES filters/models are probably as numerous as the various authors working on the subject (Berselli et al. (2005)), thus we will very brief on the subject and refer the reader to a the quite recent review Zhiyin (2015). The very first LES model is called the Leray-α model. It was used by Leray in 1934 to establish existence of weak solutions to the Navier-Stokes equations (Leray (1934)). Originally, the filtering in Leray (1934) as well as in many classical LES models was achieved by using a convolution operator $\mathcal{F}$ defined by:

$$\mathcal{F}(u)(\boldsymbol{x}) = \int\limits_{\mathbb{R}^d} u(\boldsymbol{y}) g_\delta(\boldsymbol{x}-\boldsymbol{y}) d\boldsymbol{y}, \quad \text{where} \quad g_\delta(\boldsymbol{x}) = \frac{1}{\delta^d} g\left(\frac{\boldsymbol{x}}{\delta}\right),$$

where the filter kernel g satisfies:

$$0 \le g(\boldsymbol{x}) \le 1, \qquad g(\boldsymbol{0}) = 1, \qquad \int\limits_{\mathbb{R}^d} g(\boldsymbol{x}) d\boldsymbol{x} = 1.$$

Several kernels are used in the literature, such as a low-pass filter, a box-filter or the very natural Gaussian filter $g(\boldsymbol{x}) = \pi^{-d/2} e^{-|\boldsymbol{x}|^2}$.

In figure 13 we illustrate the smoothing effect of a Gaussian kernel on an oscillating data: as expected, it preserves the high amplitude and low frequency oscillation while filtering out the high frequency and low amplitude oscillations. Such filters might therefore be ideal for our application to landscape evolution models: the small topographic perturbations will be cleaned out such that the flow routing will not be affected by it. Although convolution operators produce averages with the desired properties, they are impractical on bounded domains. The modern way of defining the Leray-α filter for bounded domains

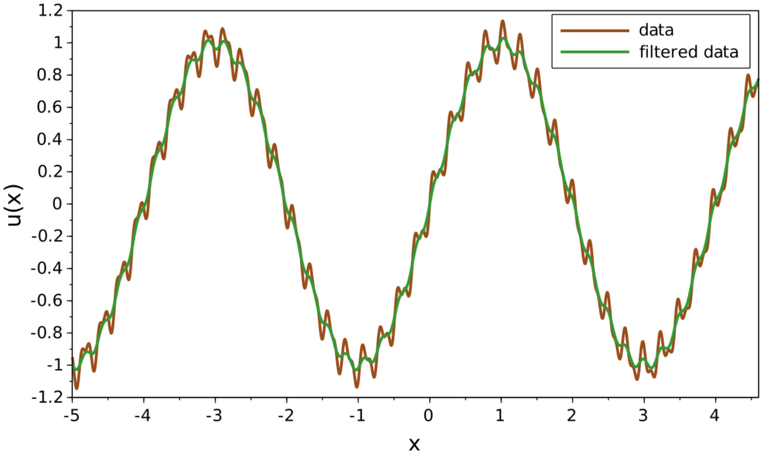

Figure 13. Illustration of the effect of the convolution by a Gaussian function

consists in using the differential filter $\mathcal{F}_\alpha$ defined by (Cheskidov et al. (2005); Guermond et al. (2003)):

$$\left|\begin{aligned} & -\alpha^2 \Delta \mathcal{F}_\alpha(u) + \mathcal{F}_\alpha(u) = u && \text{in } \Omega, \\ & \nabla \mathcal{F}_\alpha(u) \cdot \boldsymbol{n} = 0 && \text{on } \partial\Omega_{\mathcal{N}}, \\ & \mathcal{F}_\alpha(u) = 0 && \text{on } \partial\Omega_{\mathcal{D}}. \end{aligned}\right. \tag{17}$$

The filtered result $\mathcal{F}_\alpha(u)$ basically amounts to a convolution of u by the underlying Green's function (17), i.e. the filter applied to the Dirac distribution. Using a finite volume scheme $\mathcal{F}_\alpha$ we can this time easily obtain a discrete version $\mathcal{F}_{\alpha,h}$ which is one of the main reasons why we have chosen to use this filter, along with its theoretical and practical success for CFD. Notice that contrary to Cheskidov et al. (2005); Guermond et al. (2003), we use homogeneous Neumann and Dirichlet boundary conditions instead of periodic boundary conditions to simplify the treatment of the boundary. The main drawback of this choice is that our filter does not commute with differential operators. Resorting to only Dirichlet boundary conditions would have solved this issue, however from our numerical experiments we found that this can create boundary effects unless the chosen Dirichlet boundary condition is adapted to the filtered quantity. The Neumann choice avoids those difficulties without creating any practical issues, which has motivated our choice. For quantities such as the water flux for which Neumann everywhere is a more natural boundary condition, we introduce the alternative filter $\mathcal{F}_\alpha^{\mathcal{N}}$ with only Neumann boundary conditions:

$$\left|\begin{aligned} & -\alpha^2 \Delta \mathcal{F}_\alpha^{\mathcal{N}}(u) + \mathcal{F}_\alpha^{\mathcal{N}}(u) = u && \text{in } \Omega, \\ & \nabla \mathcal{F}_\alpha^{\mathcal{N}}(u) \cdot \boldsymbol{n} = 0 && \text{on } \partial\Omega. \end{aligned}\right. \tag{18}$$

4.2 Leray filtering applied to our landscape evolution model

From the numerical observations that the model governing the simultaneous evolution of sediment and water seems for large values of τ as intractable to solution as the Navier-Stokes system is for large Reynolds numbers, following the idea of LES we will now apply filtering to key parts of our model problem to obtain a more numerically stable approximate model. This means that the sediment flux used in the mass conservation equations:

$$\left| \begin{array}{ll} \dfrac{\partial h_s}{\partial t} + div\,(\boldsymbol{J}_s) = S_s & \text{in } \Omega \times]t_0, T[, \\[2ex] -\boldsymbol{J}_s \cdot \boldsymbol{n} = B_s & \text{on } \partial\Omega_{\mathcal{N}} \times]t_0, T[, \\[2ex] h_s = 0 & \text{on } \partial\Omega_{\mathcal{D}} \times]t_0, T[, \\[2ex] h_s(t = t_0) = h_{s,0} & \text{in } \Omega, \end{array} \right.$$

will now be given by:

$$\boldsymbol{J}_s = -\eta_s(h_s) s_{ref}^{-p_s} ||\nabla(h_s + b)||^{p_s} \left(\left(\frac{\mathcal{F}_\alpha^{\mathcal{N}}(q_w)}{q_{ref}} \right)^{r_s} \nabla\psi_w(h_s + b) + \nabla\psi_g(h_s + b) \right) \quad \text{in } \Omega \times]t_0, T[, \tag{19}$$

where we use the filtered water flux magnitude $\mathcal{F}_\alpha^{\mathcal{N}}(q_w)$ instead of directly using the water flux q_w. In the same way, in the water equations, we will now use the filtered topography $\mathcal{F}_\alpha(h_s + b)$ instead of the topography $h_s + b$, leading to:

$$\left| \begin{array}{ll} -div\left(k_m h_w \eta_w(h_w) s_{ref}^{-p_w} ||\nabla(\mathcal{F}_\alpha(h_s + b))||^{p_w} \nabla(\mathcal{F}_\alpha(h_s + b)) \right) = S_w & \text{in } \Omega, \\ -k_m h_w \eta_w(h_w) s_{ref}^{-p_w} ||\nabla(\mathcal{F}_\alpha(h_s + b))||^{p_w} \nabla(\mathcal{F}_\alpha(h_s + b)) \cdot n = B_w & \text{on } \partial\Omega, \end{array} \right. \tag{20}$$

with the associated water flux:

$$q_w = ||k_m h_w \eta_w(h_w) s_{ref}^{-p_w} ||\nabla(\mathcal{F}_\alpha(h_s + b))||^{p_w} \nabla(\mathcal{F}_\alpha(h_s + b))||. \tag{21}$$

Our so-called large structures simulation (LSS) for landscape evolution thus consists in solving (2)-(19)-(20)-(21). The name “large structures” originates from the fact that since we use filtering in the coupling process, the water model does not see anymore topographic details that are smaller than α, and in the same way the sediment evolution is no longer influenced by water flow details smaller than α. We have thus abandoned the idea of resolving all the scales involved in the landscape evolution problem and will only try to simulate the large sedimentary and water structures, hence the name LSS: only structures several times larger than the filter resolution α will appear in the final result.

4.3 Numerical results with filtering

Before turning to numerical experiments, one has to choose a value for the filter parameter α. Following LES principles, we know that the filter scale α corresponds to the spatial resolution of our continuous approximate model, that in practice one will want to be as small as possible. However it must naturally be resolved by the grid resolution, meaning we should have at the very least $\Delta_{xy} < \alpha$ for cartesian grids. Moreover, as we test our numerical solution against an analytic solution for the unfiltered case, we need to make the filter size go to zero at the same speed than the mesh size in order to measure a convergence. For simplicity, we have chosen to use filter parameters $\alpha = \gamma\Delta_{xy}$ with $\gamma > 1$. On figure 14 we present the convergence results obtained for the analytic test cases of section 3.1 this time using filters. Convergence is recovered with α

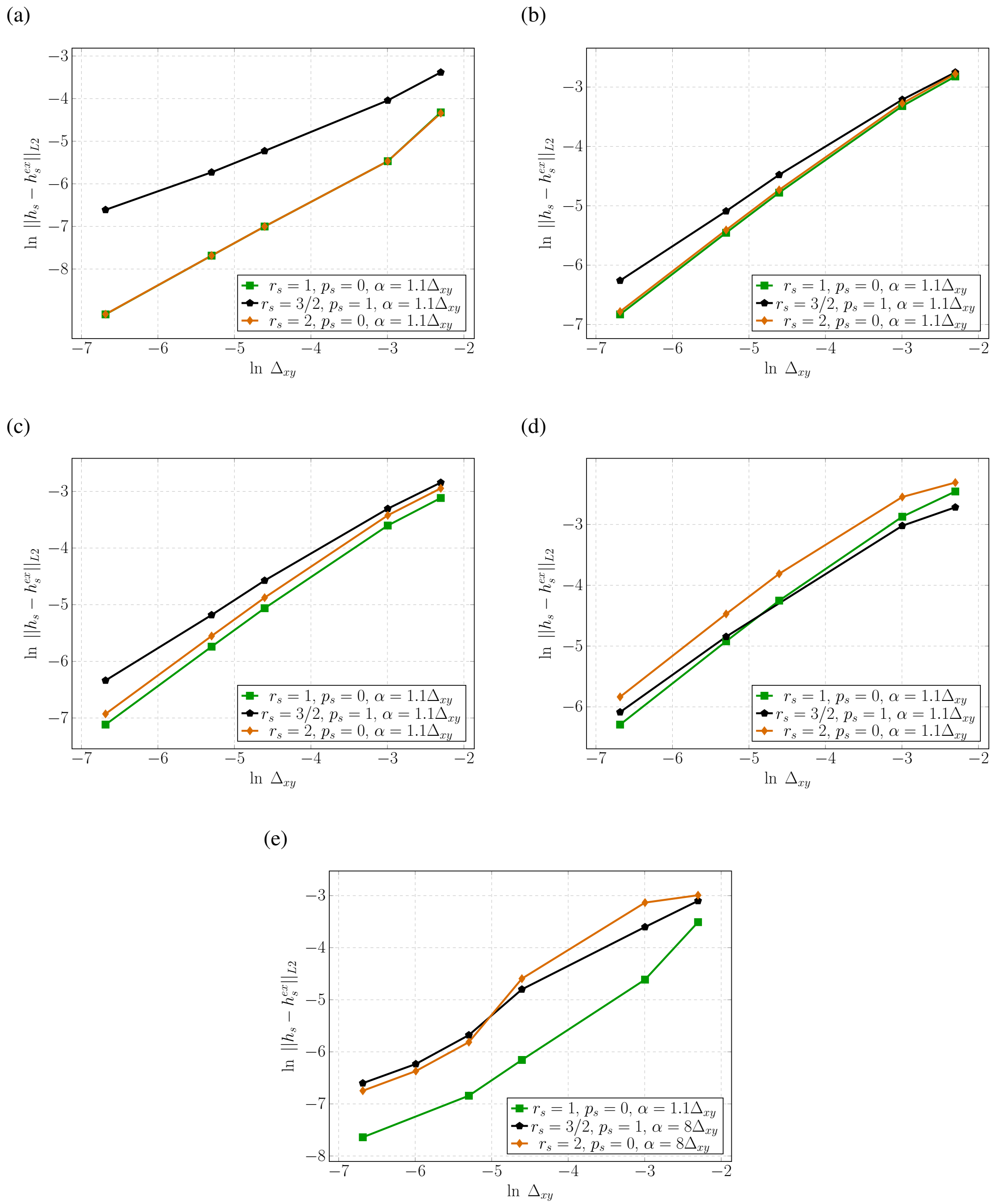

Figure 14. Convergence curves with filters. a: case k_g=50 km^2.My^{-1} and k_w=1 km^2.My^{-1}. b: case k_g=5 km^2.My^{-1} and k_w=1 km^2.My^{-1}. c: case k_g=5 km^2.My^{-1} and k_w=5 km^2.My^{-1}. d: case k_g=1 km^2.My^{-1} and k_w=5 km^2.My^{-1}. e: case k_g=1 km^2.My^{-1} and k_w=50 km^2.My^{-1}

= $1.1\Delta_{xy}$ (i.e. γ = 1.1) for every case that was already working without filter, suggesting that the LSS approach at least does not deteriorate correct results previously obtained. We also see that for the test cases with (k_g=1 km^2.My^{-1}, k_w=50 km^2.My^{-1}) convergence is now obtained for α= $8\Delta_{xy}$ (γ = 8). This choice for the ratio γ between the filter size α and the mesh size Δ_{xy} is not random. Indeed, with $\alpha = \gamma\Delta_{xy}$ when Δ_{xy} tends to zero so does the filter size and if γ is not large enough then the filtering parameter α will no longer be large enough to compensate for solver errors and numerical approximation errors. We illustrate this on figure 15.

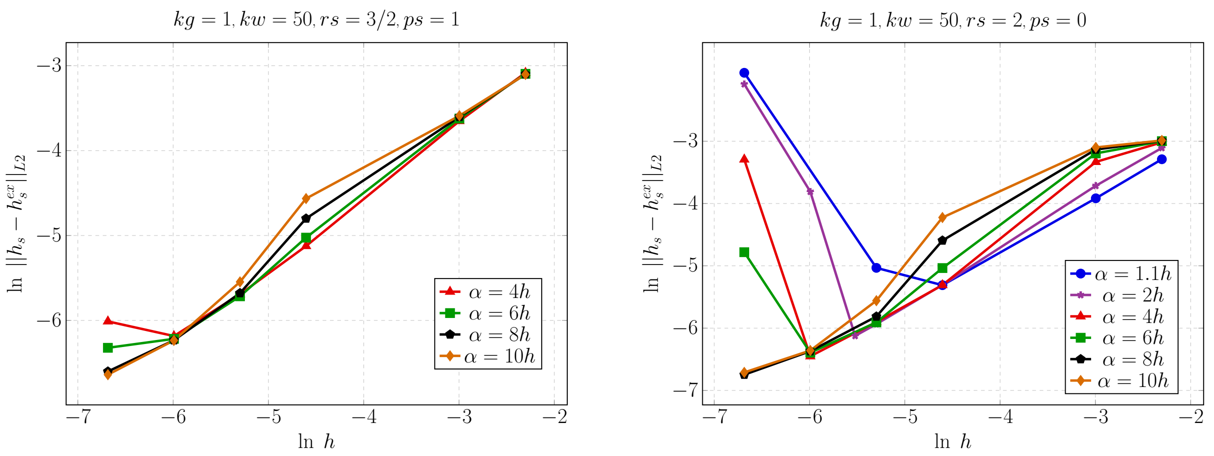

(a) (b)

Figure 15. Convergence curves for various values of the ratio α/Δ_{xy}. a: (r_s,p_s)=(3/2,1), b:(r_s,p_s)=(2,0)

Keeping in mind that we are necessarily using a fixed Newton non linear solver tolerance (1e-6 in practice) what we observe on those curves is that when the parameter α becomes smaller than some threshold value that allows to control the corresponding accumulated solver (and numerical approximation) errors, the obtained solution is no longer correct. Of course, with a larger value of γ this threshold is reached for a smaller value of Δ_{xy} which explains why once γ is large enough we can obtain the correct solution along the entire convergence curve. This threshold is likely to depend on Δ_{xy}, in the sense that for finer meshes since the size of the system is larger, so is the solver error. It is also very likely that since we expect larger values of τ to imply an increase in both the numerical approximation and solver errors, modifying τ might also probably influence this threshold value. Nevertheless the results of figure 15 exlain why we have presented results with γ =8 on figure 14: to get a correct approximation even for the finer meshes and thus a clean convergence curve. We nevertheless see on figure 15 that for more realistic mesh sizes, smaller values of γ will be more than enough to obtain the correct solution, and that using filters is not prohibitively costly in realistic configurations. We also observe that for mesh sizes allowing all the values of the ratio to γ to give a correct approximation, the error of course increases with γ, which is perfectly expected since α is our largest approximation parameter.

We finally reproduce the very same experiment that was performed on the "three rivers" test case, with sequential GMRES, parallel GMRES and sequential BiCGStab, but using a filter α= 2.2 km for Δ_{xy}=2 km. Contrary to Fig. 12, the symmetry is maintained and we obtain almost identical results for the three configurations 16. The expected impact of the filter on the simulated water flow and topography is a smoothing effect, which is what is observed when comparing for example the width of the three valleys. However, the differences remain marginal in this case.

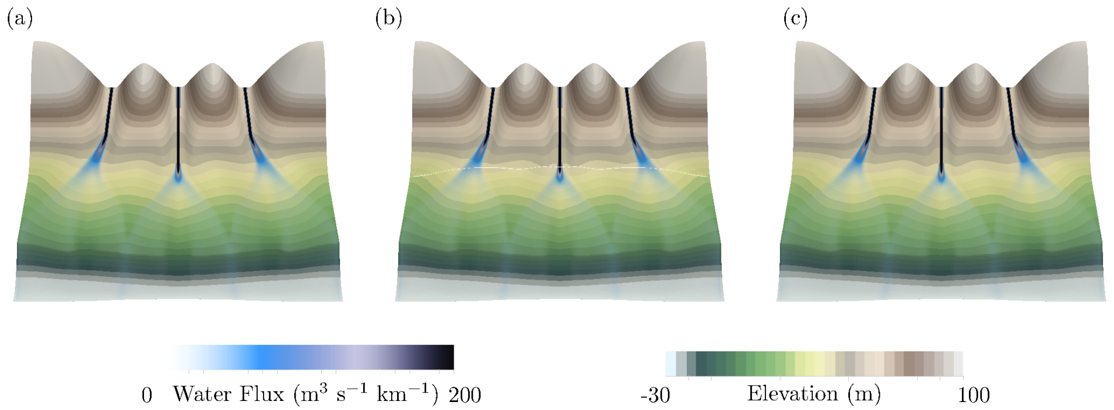

Figure 16. The "three rivers" test case with filter α= 2.2 km and Δ_{xy}=2 km. Topography and water flux after 6 My. a: sequential GMRES, b: parallel GMRES, c: sequential BiCGStab

Still on our "three rivers" test case, from our observations on the analytic cases and as we do not know the exact solution, to assess the legitimacy of our choice of filter size we analyze the behavior of the solution for various values of the filter parameter α (fixing the grid size to Δ_{xy}=2 km). Results are displayed Fig. 17. We clearly see that symmetric solutions are obtained for $\alpha > \Delta_{xy}$, while further reducing the filter parameter leads to behavior similar to the no filter case. This is first coherent with the principle of LES that the filter should control what happens below the grid scale, which can only be done if $\alpha > \Delta_{xy}$, and also a clear sign that our initial choice for the ratio $\gamma = \alpha/\Delta_{xy}$ belongs to the stable region.

4.4 Impacts of filtering on the emergence of geomorphic structures

We now consider two synthetic case studies to observe the formation of geomorphic features. The idea underlying the first test case is very simple: we re-use as our initial data the analytic solution described in section 3.1 in the case (r_s=2,p_s=0) and (k_g = 1 km^2.My^{-1}, k_w = 50 km^2.My^{-1}) the rectangular domain described in figure 3. However, instead of using the analytic source terms allowing to recover the analytic solution for all times, we simply use a constant source term (S_s =10 m.My^{-1}, S_w =1 m^3.s^{-1}km^{-2}), corresponding to a uniform constant uplift supply and a uniform constant rain.

We fix the mesh size to Δ_{xy} = 0.005 km, and we again perform the simulation over a time period of 0.25 My with maximum time steps of length Δt = 0.002 My. On figure 18, we recall the initial elevation corresponding to our analytic solution along with the final solution obtained for our now constant source terms, for various values of the filter size as well as without filters.

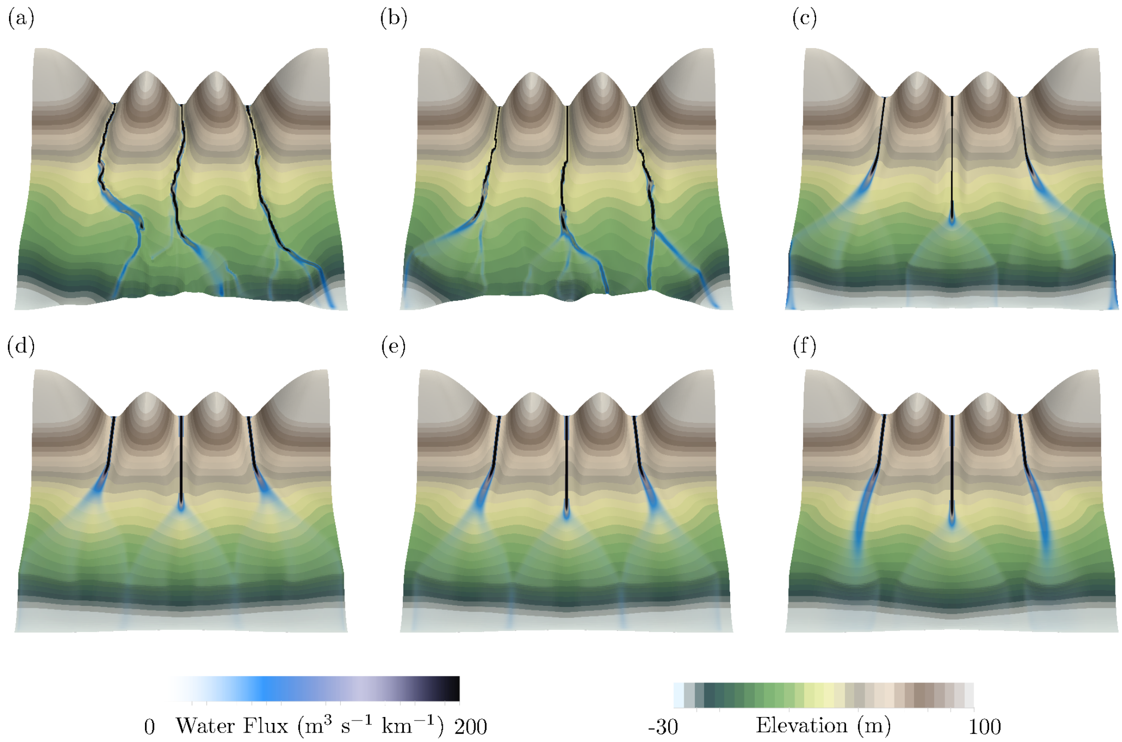

Figure 17. The "three rivers" test case with Δ_{xy}=2 km. Final topography and water flux after 6 My obtained with different values of the filter parameter α. a: no filter, b: α= 0.2 km, c: α=1 km, d: α= 2.2 km, e: α=2.5 km , f: α= 3 km

Since our new source terms are of the same magnitude than the analytic ones and since every other property of the problem is kept the same, we can anticipate using the convergence curves of figure 15 what are the filter sizes giving a correct solution (up to the approximation due to the filtering process itself). Since $\ln \Delta_{xy} \approx$ -5.298, we see on figure 15 that for our choice of Δ_{xy} we can be confident that the filter size α = 2 Δ_{xy} will give us the correct solution with a small numerical approximation error, and we use this case as a reference. Thus, the first observation on the result obtained with α = 2 Δ_{xy} is that the correct solution this time allows some legitimate geomorphic structures to appear and self organize. Those structures originate from the bumps, as if we perform the very simulation with constant source terms but without bumps, we obtain a clean uniform final state deprived of any geomoprhic complexity. With the larger filter size α = 4 Δ_{xy}, we obtain an averaged version with slightly less geomorphic complexity, illustrating the way the filter only keeps "large" structures. However for the very large filter α = 8 Δ_{xy} the approximation for Δ_{xy} = 0.005 km is too crude and we loose all the geomorphic complexity. We have checked that if we refine the mesh we recover the correct solution with the ratio α = 8 Δ_{xy}. This confirms that the uniform crude approximation obtained for α = 8 Δ_{xy} and Δ_{xy} = 0.005 km on figure 18 is as expected due to the fact that we have increased our approximation error too much by oversizing α. Now, let us consider the final solutions of figure 18 for the value

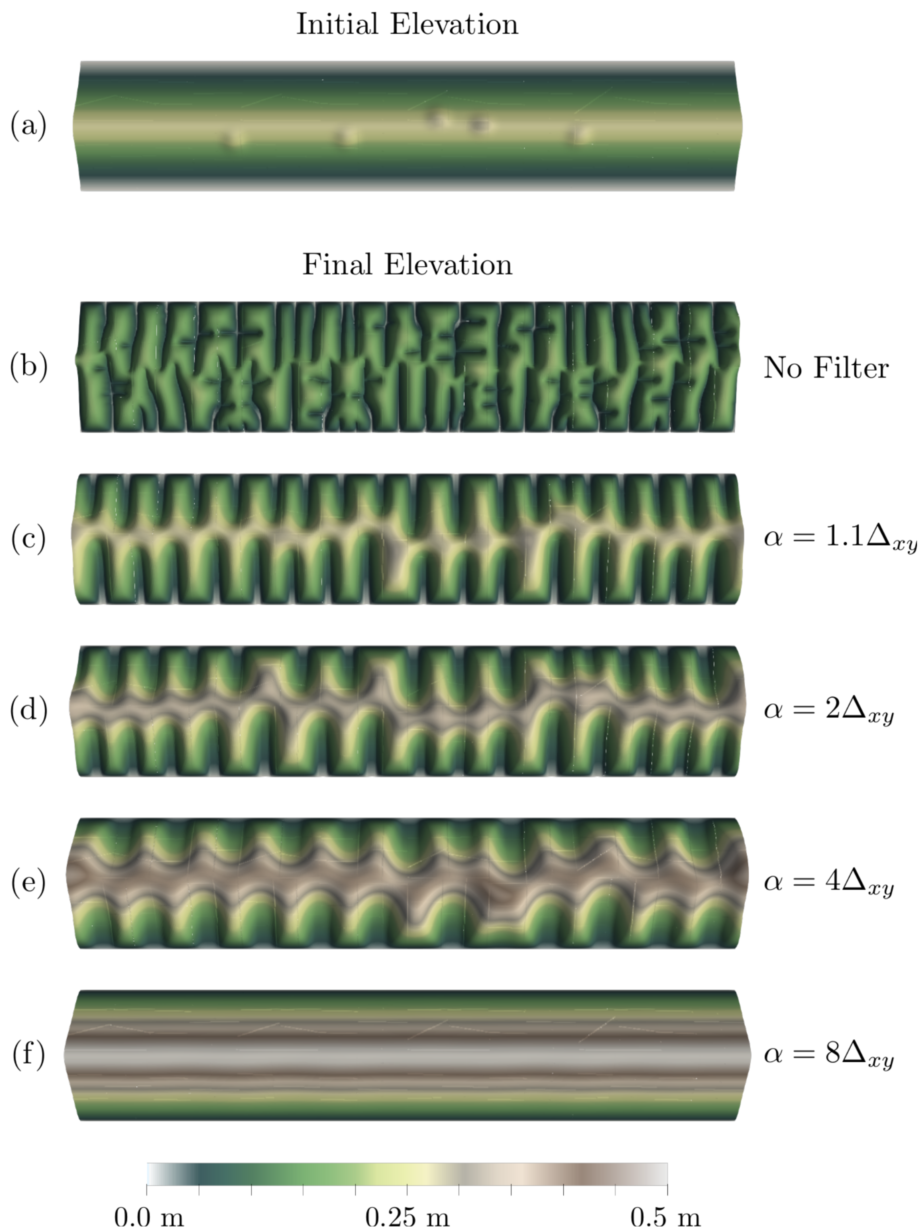

Figure 18. Results for a mesh size Δ_{xy}=5e-3 km. a : Initial elevation. Final elevation : b: no filter, c: α = 1.1 Δ_{xy}, d: α = 2 Δ_{xy}, e: α = 4 Δ_{xy}, f: α = 8 Δ_{xy}

α= 1.1 Δ_{xy} as well as without filter. Both of those results present more complexity than the reference case α = 2 Δ_{xy}. Using the convergence curves of figure 15, we expect the result obtained for α = 1.1 Δ_{xy} to belong to the hazardous region where the error level starts to increase and this solution while not completely erroneous is becoming untrustworthy. However for the solution without filter strange small structures appear and the overall topography, despite being the more complex of all, does not have any physical origin.

We now switch to a second synthetic case study. The numerical domain corresponds again to a rectangular grid but this time with dimensions $Lx = 600$ km in the x axis and $Ly = 80$ km is the y axis containing a mesh of resolution $\Delta_{xy} = 0.25$ km. The basement is b is constant equal to 0 m, while the sediment thickness h_s is initially given by a uniform in x smooth bump:

$$g(x, y) = \left| \begin{array}{ll} H \exp\left(\dfrac{-1}{1 - r_y^2}\right) & \text{for } r_y = \frac{(y-y_c)}{\delta_y} \leq 1, \\ 0 & \text{otherwise ,} \end{array} \right.$$

with $H = 20$m , $y_c = 40$ km and $\delta_y = 20$ km. This symmetry in the x direction of the initial topography is then perturbed by N_b=30 small smooth bumps randomly positioned at points (x_p, y_p):

$$g_{pert}(x, y) = \left| \begin{array}{ll} H_{pert} \exp\left(\dfrac{-1}{1 - r^2}\right) & \text{for } r^2 = \frac{(x-x_p)^2}{\delta^2} + \frac{(y-y_p)^2}{\delta^2} \leq 1, \\ 0 & \text{otherwise ,} \end{array} \right.$$

with $H_{pert} = 1$ m and $\delta = 2$ km. Rain-fall is constant in time and space (3000 mm/y) and is the unique water supply for this case. The sediment source (here we simulate a sediment production) goes from $S_s = 0$ m.My^{-1} at $y = 0$ and $y = Ly$ sides to $S_s = 100$ m.My^{-1} at $y = Ly/2 = y_c$. The variation is continuous over the whole domain following :

$$S_s(x, y) = \left| \begin{array}{ll} S_{max} \exp\left(\dfrac{-1}{1 - r_y^2}\right) & \text{for } r_y = \frac{(y-y_c)}{\delta_y} \leq 1 \\ 0 & \text{otherwise} \end{array} \right.$$

with $\delta_y = 40$ km. Model boundary conditions are fixed elevation on the sides normal to the x axis and zero gradient on the sides normal to the y axis. Models parameters controlling the non-linearity in the water-sediment coupling are set as $r_s = 2$, $p_s = 0$. Simulation takes place over the time period $T = 6$ My.

This second synthetic case study has similarities with the previous one in terms of boundary conditions, but its larger spatial-scale makes it relatively close to the case studies published in Perron et al. (2008); Armitage (2019). We display the initial topography (Fig 19-a) as well as the final topography obtained with and without filter for k_w= 5 km^2.My^{-1} and for three different k_g values. The first case considers k_g= 50 km^2.My^{-1}. The relative high k_g value compared to k_w should not favor the emergence of geomorphic structures. This is however not what we observe in the simulation performed without filter (Fig 19-b). The filter, defined by $\alpha = 0.3$ km, has a huge impact and no geomorphic structure is produced (Fig. 19-c) which is undoubtedly the correct solution. An order of magnitude smaller k_g coefficient is used for the second simulation. By decreasing k_g, the emergence of structure may be considered as a realistic result. In this case, complex structures controlled by at least one wavelength appear in the simulation performed without filter (Fig. 19-d). The effect of filter however indicates the very likely artificial origin of these structures. A residual perturbation can still be observed in the final topography (Fig. 19-e), indicating that this k_g and k_w configuration is at the transition between two regimes, the gravity-driven and the water-driven erosion regimes. In our last simulation, we have decreased k_g by a factor 5 and we indeed observe the emergence of structures even

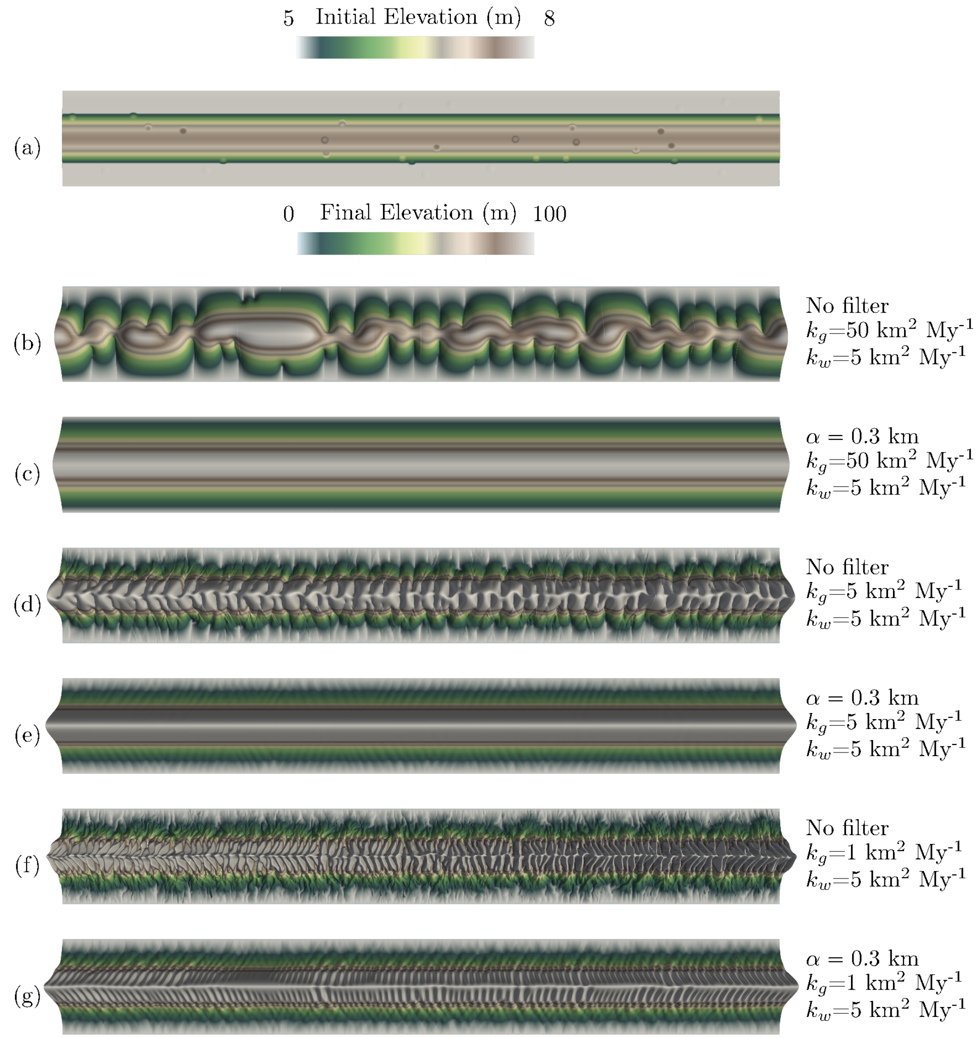

Figure 19. Final topographies obtained for three different set of diffusive coefficients, systematically tested without filter and with a filter using $\alpha = 0.3$ km. a: initial perturbed topography. b: solution without filter for (k_g, k_w)=(50,5) km^2.My^{-1}, c: solution with filter for (k_g, k_w)=(50,5) km^2.My^{-1}, d: solution without filter for (k_g, k_w)=(5,5) km^2.My^{-1}, e: solution with filter for (k_g, k_w)=(5,5) km^2.My^{-1}, f: solution without filter for (k_g, k_w)=(1,5) km^2.My^{-1}, g: solution with filter for (k_g, k_w)=(1,5) km^2.My^{-1}

when the filter is active (Fig. 19-g). Here again the impact of the filter is important and allows to keep only what we believe to be the correct structures.

This last set of simulation shows the major impact of k_g in the wavelength of the structures that can emerge from our simulation. We have also performed additional simulations (not shown here) using various k_w values for a given k_g. The results have shown that k_w must be high enough to make the structures appear, but they also show that k_g was most important than k_w in the wavelength control. We consider a dedicated study should be conducted with our model to quantify these effects but it is beyond the scope of this article. A complete study can be found in Perron et al. (2008). Even if it was performed using an other LEM model, similar conclusions with those drawn from his study are also expected in our case.

5 Discussion

We consider this work as belonging to the common effort of the scientific community to harmonize landscape evolution models. It is our belief that the most of our observations and practical recommendations can also be applied to a wider range of sediment evolution models that the one we use in this study. The implementation of the large structure simulation strategy should be accessible to every LEMs satisfying (H1), (H2) and (H3). In particular, we believe that filtering would be also very useful for the models of Perron et al. (2009); Hooshyar and Porporato (2021a); Porporato (2022) that takes the general form:

$$\left| \begin{array}{ll} \dfrac{\partial h_s}{\partial t} + div\left(\boldsymbol{J}_s\right) = S_s & \text{in } \Omega \times]t_0, T[, \\ -\boldsymbol{J}_s \cdot \boldsymbol{n} = B_s & \text{on } \partial\Omega_{\mathcal{N}} \times]t_0, T[, \\ h_s = 0 & \text{on } \partial\Omega_{\mathcal{D}} \times]t_0, T[, \\ h_s(t = t_0) = h_{s,0} & \text{in } \Omega, \end{array} \right. \qquad (22)$$

with a source given by

$$S_s = U - \kappa_w s_{ref}^{-p_{s,2}} \left(\frac{q_w}{q_{ref}}\right)^{r_s} ||\nabla(h_s + b)||^{p_{s,2}},$$

with U a sediment source term (or an uplift depending on the interpretation of b) and a sediment flux given by:

$$\boldsymbol{J}_s = -s_{ref}^{-p_s} k_g ||\nabla(h_s + b)||^{p_s} \nabla(h_s + b) \quad \text{in } \Omega \times]t_0, T[.$$

The behavior of those models is relatively close to model (2)-(9) that we have studied in detail here, with the main difference that the non-linear term $q_w^{r_s} ||\nabla(h_s + b)|^{p_s}$ appears as a reaction term rather than in a diffusive term. In particular, for $p_w = -1$ the observations on linear stability for model (22) match the conclusion of the linear stability analysis of Smith and Bretherton (1972); Smith et al. (1997). We can thus expect that model (22) will potentially suffer from similar numerical stability issues that the ones we analyzed in detail for model (2)-(9), although this certainly requires a dedicated study before drawing conclusions. In particular, several elements can help keeping the numerical errors under control: high order space and time schemes, explicit time schemes, specific solvers for the water flow model avoiding inverting a linear system, etc. Nevertheless, an immediate application of the LSS in this context consists of course in replacing q_w by its filtered version $\mathcal{F}_\alpha^{\mathcal{N}}(q_w)$ in the second member of (22) and can only improve the numerical stability. We also believe that the ξ-q model of Davy and Lague (2009) could benefit from a similar filtering strategy.

Correctly using filters requires some understanding of the scales involved in the model. Although this is not such an easy task in general, as generic guidelines concerning the relation between the filter size α and the precision of the results it is clear that the chosen filtering parameter α should resolve the main sediment structures that one wants to correctly represent in the flow, ideally fulfilling an equivalent of Nyquist's rule. For instance if an essential valley is 1 km large, then α should be several times smaller (and ideally smaller than 100 m). A good practical test consists in comparing the filtered topography $\mathcal{F}_\alpha(h_s+b)$ and the unfiltered one h_s+b. The structures of h_s+b that one wants to simulate accurately should be preserved in $\mathcal{F}_\alpha(h_s+b)$, of course in a smoother way. For instance, for a given value of α if a small topographic depression in which water could in principle flow is observed on h_s+b but is absent in $\mathcal{F}_\alpha(h_s+b)$, then if one really wants to capture water flow inside this "channel" the value of α must be reduced and the mesh refined accordingly if needed. The filter should in any case be able to clean numerical approximation and solver errors, implying that we should at the very least have $\gamma=\alpha/\Delta_{xy}>1$ to correctly resolve the targeted α spatial scale. To allow the filter to correctly clean errors that could otherwise have a destabilizing effect on the final configuration, higher values of α should probably be used for increasing values of τ. Nevertheless, our experiments illustrate that even quite small values of α allow to clean the most relevant geomorphic features.

Notice that in the present paper, we have for simplicity always used uniform meshes with a constant Δ_{xy}, hence obtaining a constant ratio $\gamma=\alpha/\Delta_{xy}$. As an immediate extension, one could resort to adaptive mesh refinement to refine the mesh in areas where τ becomes large and thus where numerical errors are more likely to be large, mitigating the increase of the system's size and thus the increase of the computational cost. In practice for constant coefficients k_g and k_w this would be equivalent to refining the mesh where water flow occurs. In addition, one could replace the constant parameter α by a space/time variable coefficient $\alpha(x,y,t)$ in an adaptive filtering strategy, where the filter size could be chosen in coherence with the local size of the structures one wants the model to be able to reproduce.

5.1 Recovering realistic landscapes

In principle, the use of filters allows to get rid of the influence of numerical noise in the solution. An apparent drawback is that for unperturbed data, complex topographies will no longer appear by themselves through the perturbations induced by either the numerical approximation or the numerical solvers. Moreover, natural landscapes exhibit some heterogeneity even under low τ regime. This suggests an ingredient is missing, and this ingredient is well-known by geologists: the heterogeneity. Indeed heterogeneity is everywhere in nature, and could be injected in such a model to make realistic looking topographies emerge. This idea is of course not new but we propose to invesigate the effect of heterogeneity in the context of the hydro-sedimentary model we use for this paper.

The first heterogeneity we consider here is injected into the k_m coefficient, reflecting variable soil rugosity. Since acquiring a roughness map adapted to the spatial scales relevant to our approach is difficult and probably not relevant for a synthetic case study, we resort to an artificial yet efficient trick, namely the Perlin noise Perlin (1985) that is often used in animated movies or video games to produce realistic looking mountains or river networks. This type of noise can easily be used to build isotropic heterogeneity maps with controlled spatial scales. We thus consider our "three rivers" test case using variable coefficients k_m in space and time (Fig. 20). Figure 20-b illustrates a typical distribution in space of the k_m coefficients when using a Perlin noise.

The range of values for the k coefficient (from $k_m = 0.01$ m.s^{-1} to $k_m = 10$ m.s^{-1}) is arbitrarily fixed while respecting realistic value ranges. Impacted by the heterogeneity in k_m, the water flow is still distributed between neighboring cells according to the gradient of the slope, but it also preferentially choose to enter the cell with the highest k_m, especially when the slopes become gentle and relatively close between neighbors. The flow then acquires a high degree of complexity despite a filter which set at $\alpha = 1.1\Delta_{xy}$ makes it possible to eliminate numerical errors.

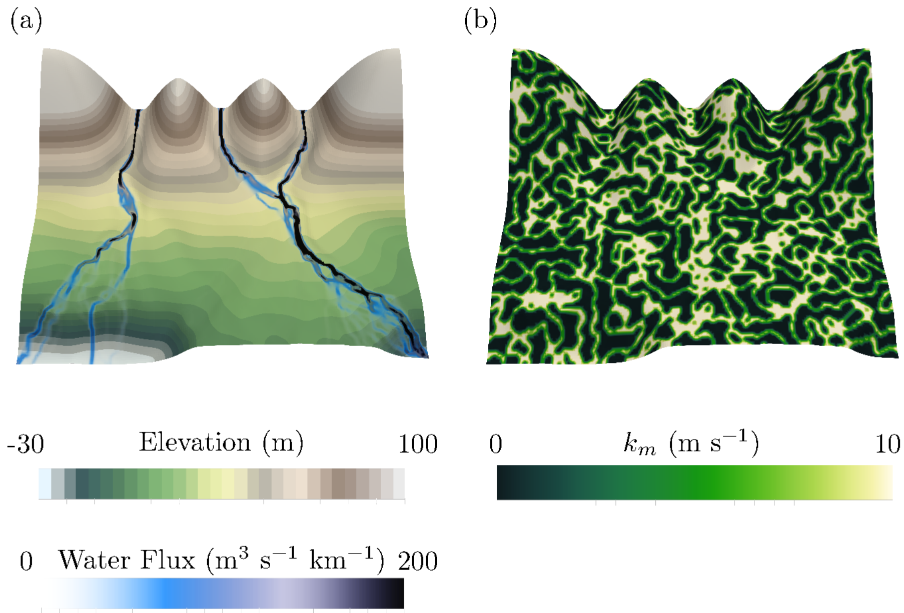

Figure 20. The “three rivers” test case with Perlin noise based coefficient k_m. a: Final (at T=6My) elevation and associated water flow with variable in space and time k_m coefficients. b: k_m coefficients at T=6My

The same approach can be applied to the other synthetic test case used in section 4.4, using α= 2 Δ_{xy}: the simulations are now performed with spatially and temporally varying k_m coefficients (the same range of k_m values is used). Figure 21-a-b shows the initial and the final state of the simulation with a special focus on the geomorphic structures produced, which are clearly more complex when comparing to the result shown in figure 18-d.

In a second time, we introduce a similar heterogeneity in the rain maps. When we use solely a rain heterogeneity incorporating the same spatial scales than in the k_m maps, the geomorphic structures produced are very similar to those obtained using only the heterogeneous k_m coefficients . The most visual satisfying result is obtained for a simulation using both variable k_m and rain maps (Fig. 21-c).

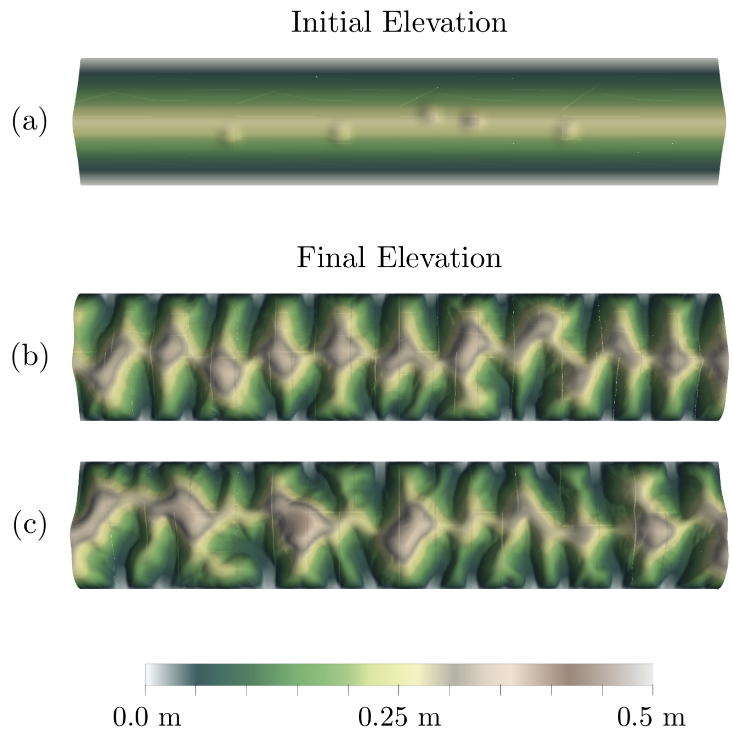

Figure 21. Results with filters and Perlin noise based k_m coefficient. a : Initial elevation, b : Final elevation with variable cofficient k_m, c: Final elevation with variable cofficient with additional Perlin noise based perturbation of rain fall

5.2 Overcoming the accumulation and flat areas limitations

In the general setting, there is no reason why the sediments should evolve in such a way that one of the sufficient conditions (8) is always fulfilled, which can lead to some non physical behavior of the GMS model (4) and thus also the pure MFD algorithms. This can occur in two obvious situations: in an accumulation area (a topographic depression) or a flat area. In principle, water arriving into an accumulation area should create a "lake" whose bathymetry will be determined by a water balance between incoming flow, infiltration and evaporation. If the surface reaches the threshold of the lake, then some water leaves the lake and the water flow restarts from the lake threshold. In flat areas, water will spread diminishing its height until the full area is covered. To reproduce those effects that are not originally taken into account, implementations the MFD algorithms all incorporate practical workarounds. Thanks to our interpretation as the discretization of a continuous model, we can easily propose a generalization of (4) that overcomes those limitations, by noticing that model (4) is in fact a simplification of the shallow water equations with friction. Indeed, appropriately choosing the friction model and assuming that the mass

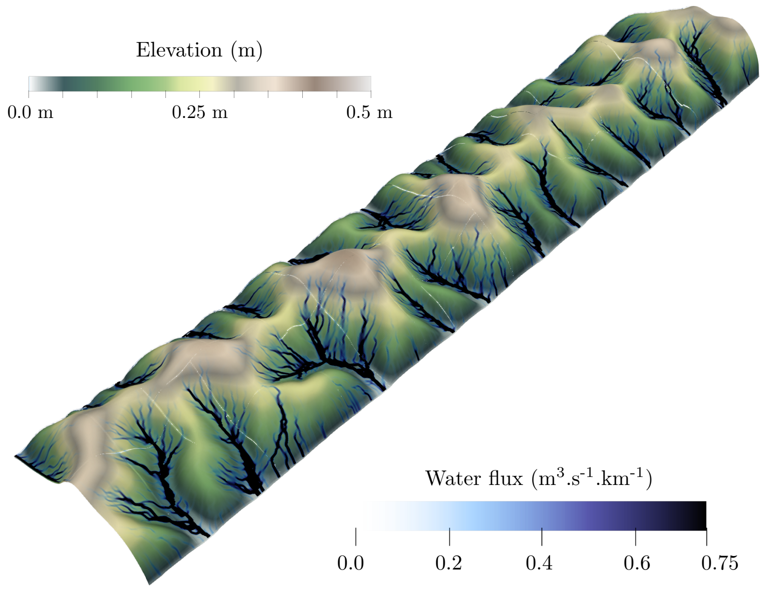

Figure 22. Front view of the result of figure 21-c

conservation of water is at steady state a quite general model arising from applying the hydrostatic approximation to the shallow water equations would be to consider (see appendix B):

$$\left|\begin{array}{ll} -div\left(k_m h_w \eta_w\left(h_w\right) s_{ref}^{-p_w} ||\nabla(h_w+h_s+b)||^{p_w} \nabla(h_w+h_s+b)\right)=S_w & \text{in } \Omega, \\ -k_m h_w \eta_w\left(h_w\right) s_{ref}^{-p_w} ||\nabla(h_w+h_s+b)||^{p_w} \nabla(h_w+h_s+b)\cdot n=B_w & \text{on } \partial\Omega_{\mathcal{N}}, \\ h_w=0 & \text{on } \partial\Omega_{\mathcal{D}}, \end{array}\right. \tag{23}$$

with the associated water flux strength:

$$q_w=\left|k_m h_w \eta_w\left(h_w\right)\right| s_{ref}^{-p_w} ||\nabla(h_w+h_s+b)||^{p_w+1}. \tag{24}$$

This is almost (4) except that it uses the hydraulic gradient instead of the topographic one.The assumption $\nabla(h_s+b)\approx\nabla(h_w+h_s+b)$ while valid on pronounced slopes is obviously not valid anymore in accumulation areas (at equilibrium, the hydraulic gradient is almost zero while the topographic gradient is large) and flat areas (where the topographic gradient is zero and the hydraulic one is not). The non-linear model (23) is thus a natural generalization of the GMS model (4) with a built-in handling of accumulation and flat areas which no longer requires practical workarounds. However, model (23) does not come without any drawbacks. The first one is that we now have to choose the water mobility function η_w, as we are solving for the water height unknown. This will both influence the repartition of water and the strength of the water flow. In the same way, the absolute value of the coefficient k_m will now impact the strength of the water flux through h_w, while only its contrasts were relevant for the GMS model (4). Thus, some fine tuning is required for (23) to produce meaningful results. The last and probably more important drawback is that (23) being non-linear in its unknown h_w, its discretization will be more involved and computationally expensive than for (4). Llet us compare the results obtained with the original GMS model (4) and with the more involved hydrologic model (23) on the "three rivers" test case, using filters in both cases. The water mobility function η_w for (23) is simply chosen as equal to one if h_w is positive and 0 otherwise.

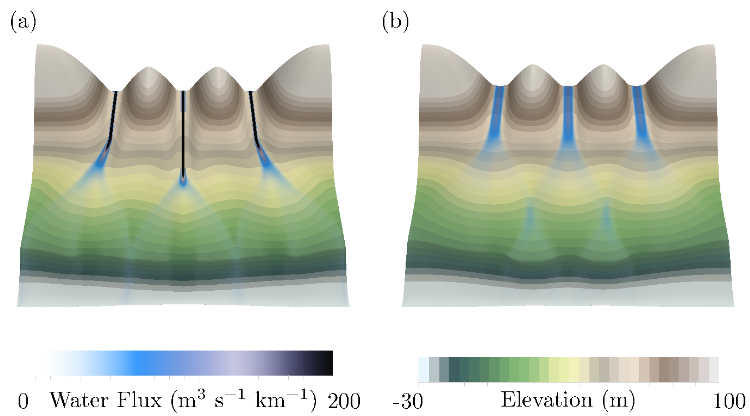

Figure 23. Comparison of models (4) and (23) on the "three rivers" test case for α=2200 m and Δ_{xy}=2000 m

As we can observe in Fig. 23, if the two models of course do not produce exactly the same results the general behavior is very similar. Even more close results could certainly be obtained by finely tuning the mobility function. We do not want to explore this any further in the present paper and simply want to illustrate that while suffering from some limitations, the GMS model (4) and thus MFD algorithms remain a very strong and attractive approximation on suitable topographies.

6 Conclusions

After illustrating the numerical instabilities arising from the self-amplification phenomenons at the core of coupling overland flow and sediment evolution models, we have proposed to mimic the LES strategy for CFD computation in the context of landscape evolution models, relying on the well known Leray-α differential filter. Numerical experiments assess that filtering produces results robust to numerical perturbations. It is our belief that this "large structures simulation" (LSS) approach goes far beyond the specific model considered here and that any LEMs could benefit from it. Indeed, experiments performed without any filtering strategy have shown that it can become extremely difficult to distinguish between the imprint of numerical errors and physical processes. Provided suitable filter parameter and mesh size are used, only the non physical heterogeneity will disappear. The apparently missing visual complexity that previously arose from numerical noise can be physcally re-introduced when heterogeneous data are considered. Similarly to LES models, we believe that a mathematical analysis and numerical analysis of the filtered model should be achievable. We hope to be able to publish such analysis in a future paper. To complete this work, we also plan to use in our next study the full model capacity in building a mutli-lithology realistic test case. Finally, pursuing the analogy with LES, an interesting perspective would be to analyze whether it is feasible to develop sub-filter models to increase the filtered model accuracy when α is quite large, in order to reduce the need for fine α and thus fine meshes and consequently the overall cost of the approach.

Code availability. All the numerical schemes used in this paper are fully described in the appendix C. Implementation was performed in code ArcaDES, which is available through the commercial simulator DionisosFlow™.

Appendix A: Derivation of analytic solutions

For simplicity, we consider in this section the special case where $b = 0$, k_w and k_g are constants, the water mobility function and coefficient k_m are both equal to one $\eta_w(h_w) = 1$ and $k_m = 1$. To ease the reading, we will not write the dimension constants s_{ref} and q_{ref}, as they are both equal to one in the chosen unit system. The sediment flux simplifies into:

$$\boldsymbol{J}_s = -\eta_s(h_s)||\nabla(h_s+b)||^{p_s}\left(q_w^{r_s}k_w\nabla(h_s+b)+k_g\nabla(h_s+b)\right) \quad \text{in } \Omega\times]t_0,T[,$$

We consider the simplified setting where $\eta_s(h_s) = 1$, which is only an approximation of the function η_s we have used everywhere else in the paper. This setting corresponds to the analytic steady state solutions studied in Smith et al. (1997). Since $\eta_s(h_s) \approx 1$ as soon as h_s is large enough, we label those solutions as "quasi steady state". We seek quasi steady state solutions that are morevoer uniform in the y variable $h_s(x,y,t) = h_{s,x}(x)$, and symmetric with respect to the axis $x = 0$, and we consider only the interval $]0, Lx/2[$. We finally assume that S_s and S_w are equal to two constants $S_{s,x}$ and $S_{w,x}$. We have consequently $\nabla(h_s+b) = \partial_x h_{s,x}\boldsymbol{e}_x$ and the water equation reduces to:

$$-\partial_x\left(h_{w,x}|\partial_x h_{s,x}|^{p_w}\partial_x h_{s,x}\right) = S_{w,x}.$$

Assuming $-\partial_x h_{s,w} > 0$ (the solution is decreasing fom the center of the domain to its boundary) this leads to $\partial_x q_{w,x} = S_{w,x}$, $q_{w,x} = -h_{w,x}|\partial_x h_{s,x}|^{p_w}\partial_x h_{s,x}$, and finally $q_{w,x} = q_w(0) + S_{w,x}x$. In the same way, the conservation of sediments reduces to:

$$-k_g\partial_x\left(|\partial_x h_{s,x}|^{p_s}\partial_x h_{s,x}\right) - \partial_x\left(k_w q_w^{r_s}|\partial_x h_{s,x}|^{p_s}\partial_x h_{s,x}\right) = S_{s,x},$$

which integrating in x leads to (using again our hypothesis on the sign of $\partial_x h_{s,x}$):

$$(\partial_x h_{s,x})^{p_s+1} = (-1)^{p_s+1}\frac{S_{s,x}x+\gamma}{k_g+k_w(q_w(0)+S_{w,x}x)^{r_s}},$$

and thus:

$$\partial_x h_{s,x} = -\frac{(S_{s,x}x+\gamma)^{\frac{1}{p_s+1}}}{(k_g+k_w(q_w(0)+S_{w,x}x)^{r_s})^{\frac{1}{p_s+1}}}.$$

To ensure the continuity of the derivatives at $x = 0$, let us assume that $\partial_x h_{s,x}(0) = 0$ and thus $\gamma = 0$, and consequently $q_w(0) = 0$. The above relation simplifies into:

$$\partial_x h_{s,x} = -(S_{s,x}x)^{\frac{1}{p_s+1}}(k_g + k_w(S_{w,x}x)^{r_s})^{-\frac{1}{p_s+1}}.$$

Notice that this is coherent with our assumption $-\partial_x h_{s,x} > 0$. The water height $h_{w,x}$ can then be obtained by setting:

$$h_{w,x} = (-1)^{p_w+1}\frac{S_{w,x}x}{\partial_x h_{s,x}^{p_w+1}} = (S_{w,x}x)(S_{s,x}x)^{\frac{-(p_w+1)}{p_s+1}}(k_g + k_w(S_{w,x}x)^{r_s})^{\frac{p_w+1}{p_s+1}},$$

which is positive as expected. At this stage, integration for $h_{s,x}$ was simpler in Smith et al. (1997) because of the absence of k_g. Indeed, for $k_g = 0$ we have:

$$\partial_x h_{s,x} = -(S_{s,x}k_w^{-1}S_{w,x}^{-r_s})^{\frac{1}{p_s+1}}x^{\frac{1-r_s}{1+p_s}},$$

immediately leading to:

$$h_{s,x} = h_{s,x}(0) - \frac{1+p_s}{2+p_s-r_s}(S_{s,x}k_w^{-1}S_{w,x}^{-r_s})^{\frac{1}{p_s+1}}x^{2+p_s-r_s}.$$

Conversely, if $k_w = 0$ (no couling between water and sediments), we have:

$$\partial_x h_{s,x} = -(k_g^{-1}S_{s,x}x)^{\frac{1}{p_s+1}},$$

and thus

$$h_{s,x} = h_{s,x}(0) - \frac{p_s+1}{p_s+2}(k_g^{-1}S_{s,x})^{\frac{1}{p_s+1}}x^{\frac{p_s+2}{p_s+1}}.$$

In the general case we need to compute:

$$h_{s,x} = h_{s,x}(0) - \int_0^x (S_{s,x}u)^{\frac{1}{p_s+1}}(k_g + k_w(S_{w,x}u)^{r_s})^{-\frac{1}{p_s+1}}du.$$

Using the variable change $v = u^{r_s}$, $u = v^{1/r_s}$ and $du = \frac{1}{r_s}v^{(1-r_s)/r_s}dv$ leads to:

$$h_{s,x} = h_{s,x}(0) - \frac{1}{r_s}S_{s,x}^{\frac{1}{p_s+1}}\int_0^{x^{r_s}} v^{\frac{(1-r_s)(p_s+1)+1}{r_s(p_s+1)}}(k_g + k_w S_{w,x}^{r_s}v)^{-\frac{1}{p_s+1}}dv,$$

which will lead to easily computable analytic solutions in particular for the special combinations of values of r_s and p_s that satisifies $(1-r_s)(p_s+1)+1 = 0$ and cancel the exponent $\frac{(1-r_s)(p_s+1)+1}{r_s(p_s+1)}$. We start by the special case $p_s = 0$ and $r_s = 2$. In this case, we have:

$$h_{s,x} = h_{s,x}(0) - \frac{1}{2}S_{s,x}\int_0^{x^2}(k_g + k_w S_{w,x}^2 v)^{-1}dv,$$

leading to:

$$h_{s,x} = h_{s,x}(0) - \frac{S_{s,x}}{2k_w S_{w,x}^2}(\ln\left(k_g + k_w S_{w,x}^2 x^2\right) - \ln(k_g)).$$

In the other cases for which $(1-r_s)(p_s+1)+1=0$, this leads to:

$$h_{s,x} = h_{s,x}(0) - \frac{1}{r_s} S_{s,x}^{\frac{1}{p_s+1}} \int_0^{x^{r_s}} (k_g + k_w S_{w,x}^{r_s} v)^{-\frac{1}{p_s+1}} dv,$$

and thus

$$h_{s,x} = h_{s,x}(0) - \frac{p_s+1}{p_s r_s} \frac{S_{s,x}^{\frac{1}{p_s+1}}}{k_w S_{w,x}^{r_s}} ((k_g + k_w S_{w,x}^{r_s} x^{r_s})^{p_s/(p_s+1)} - k_g^{p_s/(p_s+1)})$$

Apart from those cases than cancels the exponant appearing in the intregral, another interesting special case is the linear case $p_s = 0$ and $r_s = 1$ for which we have:

$$h_{s,x} = h_{s,x}(0) - \int_0^x (S_{s,x} u)(k_g + k_w(S_{w,x} u))^{-1} du,$$

which leads to:

$$h_{s,x} = h_{s,x}(0) - S_{s,x}\left(\frac{x}{k_w S_{w,x}} - \frac{k_g}{k_w^2 S_{w,x}^2} \ln|k_g + k_w S_{w,x} x| + \frac{k_g}{k_w^2 S_{w,x}^2} \ln|k_g|\right).$$

It is then easy to choose the value for $h_{s,x}(0)$ such that $h_{s,x}(Lx/2) = 0$.

Appendix B: From shallow water model to the steady-state hydrologic model (23)

Recall that the shallow water systems is given by (see Birnir et al. (2001); Peton et al. (2020)):

$$\left|\begin{array}{l} \dfrac{\partial h_w}{\partial t} + div(h_w \boldsymbol{u}_w) = 0, \\ \dfrac{\partial}{\partial t}(h_w \boldsymbol{u}_w) + div(h_w \boldsymbol{u}_w \otimes \boldsymbol{u}_w) + g h_w \nabla(h_s + b + h_w) = -\kappa_w\left(h_w, ||\nabla(h_w + h_s + b)||\right) |\boldsymbol{u}_w|^{r_w} \boldsymbol{u}_w, \end{array}\right. \tag{B1}$$

where $\boldsymbol{u}_w$ denotes the water speed, g the acceleration due to gravity, and κ_w is the friction coefficient. Then, following Peton et al. (2020) and defining $H_{s,c}$ to be the characteristic sediment height, $H_{w,c}$ the characteristic water height, L_c the characteristic domain length, T_c the characteristic time and defining the nondimensional variables:

$$\hat{h}_s = \frac{h_s}{H_{s,c}}, \quad \hat{b}_s = \frac{b}{H_{s,c}}, \quad \hat{h}_w = \frac{h_w}{H_{w,c}}, \quad \hat{\boldsymbol{u}}_w = \frac{T_c \boldsymbol{u}_w}{L_c}, \quad \hat{x} = \frac{x}{L_c}, \quad \hat{y} = \frac{y}{L_c}, \quad \hat{t} = \frac{t}{T_c},$$

we see that (B1) is equivalent to:

$$\left|\begin{array}{l} \dfrac{\partial \hat{h}_w}{\partial \hat{t}} + d\hat{i}v(\hat{h}_w \hat{\boldsymbol{u}}_w) = 0, \\[2ex] \dfrac{\partial}{\partial \hat{t}}(\hat{h}_w \hat{\boldsymbol{u}}_w) + d\hat{i}v(\hat{h}_w \hat{\boldsymbol{u}}_w \otimes \hat{\boldsymbol{u}}_w) + g\dfrac{H_{s,c} T_c^2}{L_c^2} \hat{h}_w \hat{\nabla}(\hat{h}_s + \hat{b}) + g\dfrac{H_{w,c} T_c^2}{L_c^2} \hat{h}_w \hat{\nabla}(\hat{h}_w), \\[2ex] = -\kappa_w\left(h_w, ||\nabla(h_w + h_s + b)||\right) \dfrac{L_c}{H_{w,c}} \left(\dfrac{L_c}{T_c}\right)^{r_w - 1} |\hat{\boldsymbol{u}}_w|^{r_w} \hat{\boldsymbol{u}}_w. \end{array}\right.$$

The "shallow" hypothesis corresponds to assuming that $L_c/H_{w,c} >> 1$, while the two numbers

$$F_{r,w} = \frac{L_c}{\sqrt{gH_{w,c}}T_c} \quad \text{and} \quad F_{r,s} = \frac{L_c}{\sqrt{gH_{s,c}}T_c},$$

are equivalent to Froude numbers for the water and sediment flows. For long term sediment evolution, it is reasonable to assume that $F_{r,w} << 1$ and $F_{r,s} << 1$, i.e. that gravity is the dominant phenomenon. Combined with the shallow water assumption this suggests to neglect the inertia terms in the nondimensional momentum balance, leading to the hydrostatic assumption:

$$gh_w \nabla(h_s + b + h_w) = -\kappa_w \left(h_w, ||\nabla(h_w + h_s + b)||\right) |\boldsymbol{u}_w|^{r_w} \boldsymbol{u}_w, \tag{B2}$$

Inverting formula (B2) we obtain the following expression for the water speed:

$$\boldsymbol{u}_w = -\mu_w \left(h_w, ||\nabla(h_w + h_s + b)||\right) \nabla(h_s + b + h_w), \tag{B3}$$

where

$$\mu_w \left(h_w, ||\nabla(h_w + h_s + b)||\right) = \frac{g^{\frac{1}{r_w+1}} h_w^{\frac{1}{r_w+1}}}{\kappa_w \left(h_w, ||\nabla(h_w + h_s + b)||\right)^{\frac{1}{r_w+1}}} ||\nabla(h_s + b + h_w)||^{-\frac{r_w}{r_w+1}}. \tag{B4}$$

Thus, appropriately choosing the friction model, for instance by setting $r_w = 0$ and

$$\kappa_w \left(h_w, ||\nabla(h_w + h_s + b)||\right) = \frac{gh_w}{k_m \eta_w(h_w) s_{ref}^{-p_w} ||\nabla(h_w + h_s + b)||^{p_w}}, \tag{B5}$$

and assuming that the mass conservation of water is at steady state we obtain the following quite general hydrostatic approximation to the shallow water equations:

$$\left|\begin{array}{ll} -div\left(k_m h_w \eta_w(h_w) s_{ref}^{-p_w} ||\nabla(h_w + h_s + b)||^{p_w} \nabla(h_w + h_s + b)\right) = S_w & \text{in } \Omega, \\ -k_m h_w \eta_w(h_w) s_{ref}^{-p_w} ||\nabla(h_w + h_s + b)||^{p_w} \nabla(h_w + h_s + b) \cdot n = B_w & \text{on } \partial\Omega_{\mathcal{N}}, \\ h_w = 0 & \text{on } \partial\Omega_{\mathcal{D}}, \end{array}\right.$$

with the associated water flux strength:

$$q_w = |k_m h_w \eta_w(h_w)| \, s_{ref}^{-p_w} ||\nabla(h_w + h_s + b)||^{p_w+1}.$$

Remark B.1. The friction model (B5) becomes singular when $||\nabla(h_w + h_s + b)|| = 0$. Thus, an alternate choice would be to use something like:

$$\kappa_w \left(h_w, ||\nabla(h_w + h_s + b)||\right) = \frac{gh_w}{k_m \eta_w(h_w)(\beta + s_{ref}^{-p_w} ||\nabla(h_w + h_s + b)||^{p_w})},$$

for some $\beta > 0$ (the same holds for function η_w such that $\eta(0) = 0$). This alternate choice is probably more physical, as the term in $s_{ref}^{-p_w} ||\nabla(h_w + h_s + b)||^{p_w}$ can be interpreted as modeling some deceleration in accumulation areas. We have chosen to use (B5) to be as close as possible to the MFD algorithms of the literature.

Appendix C: Finite volume discretization

In this section we describe the full finite volume discretization of system (2)-(19)-(20)-(21). Let Ω be a bounded polyhedral connected domain of $\mathbb{R}^2$, whose boundary is denoted $\partial\Omega = \overline{\Omega} \setminus \Omega$. We recall the usual finite volume notations describing a mesh $\mathcal{M} = (\mathcal{T}, \mathcal{F})$ of Ω. The set of the cells of the mesh $\mathcal{T}$ is a finite family of connected open disjoint polygonal subsets of Ω, such that $\overline{\Omega} = \cup_{K\in\mathcal{T}} \overline{K}$. For any $K \in \mathcal{T}$, we denote by $|K|$ the measure of $|K|$, by $\partial K = \overline{K} \setminus K$ the boundary of K, by ρ_K its diameter and by $\boldsymbol{x}_K$ its barycenter. The set of faces of the mesh $\mathcal{F}$ is a finite family of disjoint subsets of $\mathbb{R}^2$ included in $\overline{\Omega}$ such that, for all $\sigma \in \mathcal{F}$, its measure is denoted $|\sigma|$, its diameter h_σ and its barycenter $\boldsymbol{x}_\sigma$. For any $K \in \mathcal{T}$, the faces of cells K corresponds to the subset $\mathcal{F}_K$ of $\mathcal{F}$ such that $\partial K = \cup_{\sigma\in\mathcal{F}_K} \overline{\sigma}$. Then, for any face $\sigma \in \mathcal{F}$, we denote by $\mathcal{T}_\sigma = \{K \in \mathcal{T} \mid \sigma \in \mathcal{F}_K\}$ the cells of which σ is a face. Next, for all cell $K \in \mathcal{T}$ and all face $\sigma \in \mathcal{F}_K$ of cell K, we denote by $\boldsymbol{n}_{K,\sigma}$ the unit normal vector to σ outward to K, and $d_{K,\sigma} = |\boldsymbol{x}_\sigma - \boldsymbol{x}_K|$. The set of boundary faces is denoted $\mathcal{F}_{ext}$, while interior faces are denoted $\mathcal{F}_{int}$. Finally for any $\sigma \in \mathcal{F}_{int}$, whenever the context is clear we will denote by K and L the two cells forming $\mathcal{T}_\sigma = \{K, L\}$, as well as $d_{KL} = |\boldsymbol{x}_K - \boldsymbol{x}_L|$. This for instance allows when looping over the faces σ of cell K to denote by L the other face of σ without resorting to a too heavy notation. To avoid any confusion with water and sediment heights, $\epsilon = \max_{K\in\mathcal{T}} \rho_K$ will denote the mesh size. For any continuous quantity u, its discrete counterpart will be denoted $u_\mathcal{T} = ((u_K)_{K\in\mathcal{T}}, (u_\sigma)_{\sigma\in\mathcal{F}_{ext}})$ where for any $K \in \mathcal{T}$ u_K is the constant approximation of u in cell K while for any $\sigma \in \mathcal{F}_{ext}$ u_σ is the constant approximation of u over face σ.

In the following we will assume that the mesh is orthogonal, i.e. there exists a family of centroids $(\overline{\boldsymbol{x}}_K)_{K\in\mathcal{T}}$ such that:

$$\overline{\boldsymbol{x}}_K \in K \quad \forall K \in \mathcal{T} \quad \text{and} \quad \frac{\overline{\boldsymbol{x}}_L - \overline{\boldsymbol{x}}_K}{|\overline{\boldsymbol{x}}_L - \overline{\boldsymbol{x}}_K|} = \boldsymbol{n}_{K,\sigma} \quad \text{for} \quad \sigma \in \mathcal{F}_{int},\, \sigma = \{K, L\}$$

and let us denote $\overline{\boldsymbol{x}}_\sigma$ the orthogonal projection of $\overline{\boldsymbol{x}}_K$ to the hyperplane containing σ for any $\sigma \in \mathcal{F}_K$ and any $K \in \mathcal{T}$ with $\overline{d}_{K,\sigma} = |\overline{\boldsymbol{x}}_K - \overline{\boldsymbol{x}}_\sigma|$, as well as $\overline{d}_{KL} = |\overline{\boldsymbol{x}}_K - \overline{\boldsymbol{x}}_L|$. Then, one can use a two-point finite volume scheme to discretize diffusion operators with scalar diffusion coefficients (no tensors). We also assume that the mesh is compatible with the boundary decomposition, i.e. there exists subsets $\mathcal{F}_{ext}^{\mathcal{N}}$ and $\mathcal{F}_{ext}^{\mathcal{D}}$ such that:

$$\overline{\partial\Omega_\mathcal{N}} = \bigcup_{\sigma\in\mathcal{F}_{ext}^{\mathcal{N}}} \overline{\sigma} \quad \text{and} \quad \overline{\partial\Omega_\mathcal{D}} = \bigcup_{\sigma\in\mathcal{F}_{ext}^{\mathcal{D}}} \overline{\sigma}.$$

Notice that all our simulations without filters employs the same numerical schemes but of course replacing the filtered values by the original ones.

Leray-α filtering equation:

Using the two-point flux approximation (TPFA) the approximate filter $\mathcal{F}_{\alpha,h}$ is defined for

$$u_\mathcal{T} = ((u_K)_{K\in\mathcal{T}}, (u_\sigma)_{\sigma\in\mathcal{F}_{ext}})$$

by

$$\mathcal{F}_{\alpha,h}(u_\mathcal{T}) = ((\mathcal{F}_{\alpha,K}(u_\mathcal{T}))_{K\in\mathcal{T}}, (\mathcal{F}_{\alpha,\sigma}(u_\mathcal{T}))_{\sigma\in\mathcal{F}_{ext}}),$$

where:

$$
\left|
\begin{aligned}
&\alpha^2 \sum_{\sigma\in\mathcal{F}_K\cap\mathcal{F}_{int}} \frac{|\sigma|}{\overline{d}_{KL}}(\mathcal{F}_{\alpha,K}(u_\mathcal{T})-\mathcal{F}_{\alpha,L}(u_\mathcal{T})) + |K|\mathcal{F}_{\alpha,K}(u_\mathcal{T}) = |K|u_K \quad \text{for all } K\in\mathcal{T},\\
&\mathcal{F}_{\alpha,\sigma}(u_\mathcal{T}) = \mathcal{F}_{\alpha,K}(u_\mathcal{T}) \quad \text{for all } K\in\mathcal{T} \text{ and all } \sigma\in\mathcal{F}_K\cap\mathcal{F}^{\mathcal{N}}_{ext},\\
&\mathcal{F}_{\alpha,\sigma}(u_\mathcal{T}) = 0 \quad \text{for all } K\in\mathcal{T} \text{ and all } \sigma\in\mathcal{F}_K\cap\mathcal{F}^{\mathcal{D}}_{ext}.
\end{aligned}
\right.
\tag{C1}
$$

The discrete Neumann filter $\mathcal{F}^{\mathcal{N}}_{\alpha,h}$ of course satisfies (C1) but with Neumann boundary conditions on every $\sigma\in\mathcal{F}_{ext}$.

Sediment mass conservation equations:

We now assume that the time interval $]0,T[$ is subdivided into N_T subintervals $]t_n,t_{n+1}[$, where $t_0=0$ and $t_{N_T+1}=T$. We denote $\Delta t^n = t_{n+1}-t_n$. The discrete quantities associated with time t_n will be denoted as usual with a superscript n. The TPFA finite volume scheme for the mass conservation of sediments (2) for the flux (19) is given by:

$$
\left|
\begin{aligned}
&\frac{|K|}{\Delta t^n}(h^{n+1}_{s,K}-h^n_{s,K}) + \sum_{\sigma\in\mathcal{F}_K\cap\mathcal{F}_{int}} \frac{|\sigma|}{\overline{d}_{KL}s^{p_w}_{ref}}\eta^{n+1}_{s,\sigma}\Delta\Psi^{n,n+1}_{KL} + \sum_{\sigma\in\mathcal{F}_K\cap\mathcal{F}^{\mathcal{D}}_{ext}} \frac{|\sigma|}{\overline{d}_{K\sigma}s^{p_w}_{ref}}\eta^{n+1}_{s,\sigma}\Delta\Psi^{n,n+1}_{K\sigma},\\
&-\sum_{\sigma\in\mathcal{F}_K\cap\mathcal{F}^{\mathcal{N}}_{ext}} |\sigma|B^{n+1}_{s,\sigma} = |K|S^n_{s,K} \quad \text{for all } K\in\mathcal{T},\\
&h^{n+1}_{s,\sigma}+b^{n+1}_\sigma = h^{n+1}_{s,K}+b^{n+1}_K+\boldsymbol{G}^{n+1}_{s,K}\cdot(\overline{\boldsymbol{x}}_\sigma-\overline{\boldsymbol{x}}_K) \quad \text{for all } K\in\mathcal{T} \text{ and all } \sigma\in\mathcal{F}_K\cap\mathcal{F}^{\mathcal{N}}_{ext},\\
&h^{n+1}_{s,\sigma} = 0 \quad \text{for all } \sigma\in\mathcal{F}^{\mathcal{D}}_{ext},
\end{aligned}
\right.
\tag{C2}
$$

where

$$
\Delta\Psi^{n,n+1}_{KL} = (q^{n+1}_{w,\sigma})^{r_s}||\boldsymbol{G}^{\dagger,n+1}_{s,\sigma}||^{p_{s,1}}(\psi_w(h_{s,K}+b_K)-\psi_w(h_{s,L}+b_L)) + ||\boldsymbol{G}^{\dagger,n+1}_{s,\sigma}||^{p_{s,2}}(\psi_g(h_{s,K}+b_K)-\psi_g(h_{s,L}+b_L)), \tag{C3}
$$

and

$$
\Delta\Psi^{n,n+1}_{K\sigma} = (q^{n+1}_{w,\sigma})^{r_s}||\boldsymbol{G}^{\dagger,n+1}_{s,\sigma}||^{p_{s,1}}(\psi_w(h_{s,K}+b_K)-\psi_w(h_{s,\sigma}+b_\sigma)) + ||\boldsymbol{G}^{\dagger,n+1}_{s,\sigma}||^{p_{s,2}}(\psi_g(h_{s,K}+b_K)-\psi_g(h_{s,\sigma}+b_\sigma)), \tag{C4}
$$

where the mobility $\eta^{n+1}_{s,\sigma}$ is upwinded using $\Delta\Psi^{n,n+1}_{KL}$ for $\sigma\in\mathcal{F}_{int}$:

$$
\eta^{n+1}_{s,\sigma} = \left|
\begin{aligned}
&\eta_s(h^{n+1}_{s,K}) \quad \text{if } \Delta\Psi^{n,n+1}_{KL}\geq 0,\\
&\eta_s(h^{n+1}_{s,L}) \quad \text{if } \Delta\Psi^{n,n+1}_{KL}< 0,
\end{aligned}
\right.
\tag{C5}
$$

and using $\Delta\Psi^{n,n+1}_{K\sigma}$ for $\sigma\in\mathcal{F}^{\mathcal{D}}_{ext}$:

$$
\eta^{n+1}_{s,\sigma} = \left|
\begin{aligned}
&\eta_s(h^{n+1}_{s,K}) \quad \text{if } \Delta\Psi^{n,n+1}_{K\sigma}\geq 0,\\
&\eta_s(h^{n+1}_{s,\sigma}) \quad \text{if } \Delta\Psi^{n,n+1}_{K\sigma}< 0,
\end{aligned}
\right.
\tag{C6}
$$

and where the filtered water flux magnitude is approximated by the harmonic mean whenever possible and the mean value otherwise:

$$q_{w,\sigma}^{n+1} = \left| \begin{array}{ll} \mathcal{F}_{\alpha,K}^{\mathcal{N}}(q_{w,\mathcal{T}}^{n+1}) & \text{if } \sigma \in \mathcal{F}_{ext}^{\mathcal{D}} \\ \dfrac{\overline{d}_{KL}\mathcal{F}_{\alpha,K}^{\mathcal{N}}(q_{w,\mathcal{T}}^{n+1})\mathcal{F}_{\alpha,L}^{\mathcal{N}}(q_{w,\mathcal{T}}^{n+1})}{\mathcal{F}_{\alpha,K}^{\mathcal{N}}(q_{w,\mathcal{T}}^{n+1})\overline{d}_{L\sigma} + \mathcal{F}_{\alpha,L}^{\mathcal{N}}(q_{w,\mathcal{T}}^{n+1})\overline{d}_{K\sigma}} & \text{if } \sigma \in \mathcal{F}_{int} \text{ and } \mathcal{F}_{\alpha,K}^{\mathcal{N}}(q_{w,\mathcal{T}}^{n+1}) > 0 \text{ and } \mathcal{F}_{\alpha,L}^{\mathcal{N}}(q_{w,\mathcal{T}}^{n+1}) > 0, \\ \dfrac{1}{2}(\mathcal{F}_{\alpha,K}^{\mathcal{N}}(q_{w,\mathcal{T}}^{n+1}) + \mathcal{F}_{\alpha,L}^{\mathcal{N}}(q_{w,\mathcal{T}}^{n+1})) & \text{if } \sigma \in \mathcal{F}_{int} \text{ and } \mathcal{F}_{\alpha,K}^{\mathcal{N}}(q_{w,\mathcal{T}}^{n+1}) = 0 \text{ or } \mathcal{F}_{\alpha,L}^{\mathcal{N}}(q_{w,\mathcal{T}}^{n+1}) = 0. \end{array} \right. \tag{C7}$$

The discrete full topographic gradient is given for any cell $K \in \mathcal{T}$ by:

$$\boldsymbol{G}_{s,K}^{n} = \frac{1}{|K|} \sum_{\sigma \in \mathcal{F}_K \cap \mathcal{F}_{int}} \frac{|\sigma|}{\overline{d}_{KL}} (h_{s,L}^{n} + b_L^{n} - h_{s,K}^{n} - b_K^{n})(\boldsymbol{x}_\sigma - \boldsymbol{x}_K)$$

$$+ \frac{1}{|K|} \sum_{\sigma \in \mathcal{F}_K \cap \mathcal{F}_{ext}} \frac{|\sigma|}{\overline{d}_{K\sigma}} (h_{s,\sigma}^{n} + b_\sigma^{n} - h_{s,K}^{n} - b_K^{n})(\boldsymbol{x}_\sigma - \boldsymbol{x}_K),$$

while its stabilized version $\boldsymbol{G}_{s,\sigma}^{\dagger,n}$ is given by $\boldsymbol{G}_{s,\sigma}^{\dagger,n} = \boldsymbol{G}_{s,\sigma}^{n} + \boldsymbol{R}_{s,\sigma}^{n}$ with:

$$\boldsymbol{G}_{s,\sigma}^{n} = \left| \begin{array}{ll} \dfrac{1}{2}(\boldsymbol{G}_{s,K}^{n} + \boldsymbol{G}_{s,L}^{n}) & \text{if } \mathcal{T}_\sigma = \{K, L\}, \\ \boldsymbol{G}_{s,K}^{n} & \text{if } \mathcal{T}_\sigma = \{K\}, \end{array} \right. \tag{C8}$$

as well as:

$$\boldsymbol{R}_{s,\sigma}^{n} = \left| \begin{array}{ll} \dfrac{1}{\overline{d}_{KL}^{2}} \left(h_{s,L}^{n} + b_L^{n} - h_{s,K}^{n} - b_K^{n} - \boldsymbol{G}_{s,\sigma}^{n} \cdot (\overline{\boldsymbol{x}}_L - \overline{\boldsymbol{x}}_K)\right)(\overline{\boldsymbol{x}}_L - \overline{\boldsymbol{x}}_K) & \text{if } \mathcal{T}_\sigma = \{K, L\}, \\ \dfrac{1}{\overline{d}_{K\sigma}^{2}} \left(h_{s,\sigma}^{n} + b_\sigma^{n} - h_{s,K}^{n} - b_K^{n} - \boldsymbol{G}_{s,\sigma}^{n} \cdot (\overline{\boldsymbol{x}}_\sigma - \overline{\boldsymbol{x}}_K)\right)(\overline{\boldsymbol{x}}_\sigma - \overline{\boldsymbol{x}}_K) & \text{if } \mathcal{T}_\sigma = \{K\}. \end{array} \right. \tag{C9}$$

Water equations:

The finite volume scheme for the water equations (20)-(21) is simply obtained by applying the corrected MFD algorithm of Coatléven (2020) on the filtered topography and reconstructing a consistent water flux by setting $q_K^{n+1} = ||\boldsymbol{Q}_K^{n+1}||$ with:

$$\boldsymbol{Q}_K^{n+1} = \sum_{\sigma \in \mathcal{F}_K \cap \mathcal{F}_{int}, \mathcal{F}_{\alpha,K}(h_{s,\mathcal{T}}^{n} + b_{\mathcal{T}}^{n}) > \mathcal{F}_{\alpha,L}(h_{s,\mathcal{T}}^{n} + b_{\mathcal{T}}^{n})} \frac{\tau_{KL}^{n,n+1}\widetilde{q}_K^{n+1}}{|K| s_K^{n,n+1}} (\mathcal{F}_{\alpha,K}(h_{s,\mathcal{T}}^{n} + b_{\mathcal{T}}^{n}) - \mathcal{F}_{\alpha,L}(h_{s,\mathcal{T}}^{n} + b_{\mathcal{T}}^{n}))(\boldsymbol{x}_\sigma - \boldsymbol{x}_K) -$$

$$\sum_{\sigma \in \mathcal{F}_K \cap \mathcal{F}_{int}, \mathcal{F}_{\alpha,K}(h_{s,\mathcal{T}}^{n} + b_{\mathcal{T}}^{n}) < \mathcal{F}_{\alpha,L}(h_{s,\mathcal{T}}^{n} + b_{\mathcal{T}}^{n})} \frac{\tau_{KL}^{n,n+1}\widetilde{q}_L^{n+1}}{|K| s_L^{n,n+1}} (\mathcal{F}_{\alpha,L}(h_{s,\mathcal{T}}^{n} + b_{\mathcal{T}}^{n}) - \mathcal{F}_{\alpha,K}(h_{s,\mathcal{T}}^{n} + b_{\mathcal{T}}^{n}))(\boldsymbol{x}_\sigma - \boldsymbol{x}_K)$$

$$- \sum_{\sigma \in \mathcal{F}_K \cap \mathcal{F}_{ext}} |\sigma| B_{w,\sigma}^{n+1}, \tag{C10}$$

and

$$\left|\begin{aligned}
&\widetilde{q}_K^{n+1} - \sum_{\sigma\in\mathcal{F}_K\cap\mathcal{F}_{int},\mathcal{F}_{\alpha,K}(h^n_{s,\mathcal{T}}+b^n_{\mathcal{T}})<\mathcal{F}_{\alpha,L}(h^n_{s,\mathcal{T}}+b^n_{\mathcal{T}})} \tau_{KL}^{n,n+1}\frac{\widetilde{q}_L^{n+1}}{s_L^{n,n+1}}\left(\mathcal{F}_{\alpha,L}(h^n_{s,\mathcal{T}}+b^n_{\mathcal{T}}) - \mathcal{F}_{\alpha,K}(h^n_{s,\mathcal{T}}+b^n_{\mathcal{T}})\right)\\
&- \sum_{\sigma\in\mathcal{F}_K\cap\mathcal{F}_{ext}} |\sigma| B_{w,\sigma}^{n+1} = |K| S_{w,K}^n \quad \text{for all } K\in\mathcal{T},\\
&s_K^{n,n+1} = \sum_{\sigma\in\mathcal{F}_K\cap\mathcal{F}_{int},\mathcal{F}_{\alpha,K}(h^n_{s,\mathcal{T}}+b^n_{\mathcal{T}})\geq\mathcal{F}_{\alpha,L}(h^n_{s,\mathcal{T}}+b^n_{\mathcal{T}})} \tau_{KL}^{n,n+1}\left(\mathcal{F}_{\alpha,K}(h^n_{s,\mathcal{T}}+b^n_{\mathcal{T}}) - \mathcal{F}_{\alpha,L}(h^n_{s,\mathcal{T}}+b^n_{\mathcal{T}})\right)\\
&\tau_{KL}^{n,n+1} = \frac{|\sigma| k_{m,\sigma}^{n+1}}{\overline{d}_{KL} s_{ref}^{p_w}} ||\boldsymbol{G}^n_{\mathcal{F},s,\sigma}||^{p_w},
\end{aligned}\right. \tag{C11}$$

where

$$\boldsymbol{G}^n_{\mathcal{F},s,\sigma} = \left|\begin{array}{ll} \frac{1}{2}(\boldsymbol{G}^n_{\mathcal{F},s,K} + \boldsymbol{G}^n_{\mathcal{F},s,L}) & \text{if } \mathcal{T}_\sigma = \{K,L\},\\ \boldsymbol{G}^n_{\mathcal{F},s,K} & \text{if } \mathcal{T}_\sigma = \{K\}, \end{array}\right. \tag{C12}$$

and the gradient of the filtered topography is of course given by:

$$\boldsymbol{G}^n_{\mathcal{F},s,K} = \frac{1}{|K|}\sum_{\sigma\in\mathcal{F}_K\cap\mathcal{F}_{int}} \frac{|\sigma|}{\overline{d}_{KL}}(\mathcal{F}_{\alpha,L}(h^n_{s,\mathcal{T}}+b^n_{\mathcal{T}}) - \mathcal{F}_{\alpha,K}(h^n_{s,\mathcal{T}}+b^n_{\mathcal{T}}))(\boldsymbol{x}_\sigma - \boldsymbol{x}_K)$$

$$+\frac{1}{|K|}\sum_{\sigma\in\mathcal{F}_K\cap\mathcal{F}_{ext}} \frac{|\sigma|}{\overline{d}_{K\sigma}}(\mathcal{F}_{\alpha,\sigma}(h^n_{s,\mathcal{T}}+b^n_{\mathcal{T}}) - \mathcal{F}_{\alpha,K}(h^n_{s,\mathcal{T}}+b^n_{\mathcal{T}}))(\boldsymbol{x}_\sigma - \boldsymbol{x}_K).$$

Author contributions. Julien Coatléven: conceptualization, writing, software, simulations. Benoit Chauveau: writing, software, simulations

Competing interests. Both the authors are core developers of the ArcaDES simulator supporting DionisosFlow™, a commercial stratigraphic simulator.

Acknowledgements. The authors would like to thank John J. Armitage and Didier Granjeon for their careful reading of the present paper.

References

Armitage, J. J.: Short communication: flow as distributed lines within the landscape, Earth Surface Dynamics, 7, 67–75, https://doi.org/10.5194/esurf-7-67-2019, 2019.

Balay, S., Gropp, W., McInnes, L. C., and Smith, B. F.: PETSc, the portable, extensible toolkit for scientific computation, Argonne National Laboratory, 2, 1998.

Bardos, C.: Problèmes aux limites pour les équations aux dérivées partielles du premier ordre à coefficients réels ; Théorèmes d'approximation ; Application à l'équation de transport, Ann. Sci. Ec. Norm. Sup. Ser. 4, Vol. 3, pp. 185-233, 1970.

Berselli, L. C., Iliescu, T., and Layton, W. J.: Mathematics of Large Eddy Simulation of Turbulent Flows, Springer Berlin, Heidelberg, 2005.

Birnir, B., Smith, T. R., and Merchant, G. E.: The scaling of fluvial landscapes, Comput. Geosci., 27(10), 1189–1216, https://doi.org/https://doi.org/10.1016/S0098-3004(01)00022-X, 2001.

Bonetti, S., Bragg, A. D., and Porporato, A.: On the theory of drainage area for regular and non-regular points, Proc. R. Soc. A 474: 20170693, 2018.

Bonetti, S., Hooshyar, M., Camporeale, C., and Porporato, A.: Channelization cascade in landscape evolution, PNAS, Vol. 117(3), pp. 1375-1382, 2020.

Cheskidov, A., Olson, E., Holm, D., and Titi, E.: On a Leray-α model of turbulence, Proc. R. Soc. Lond. Ser. A Math. Phys. Eng. Sci., Vol. 146, pp. 1-21, 2005.

Coatléven, J.: Some multiple flow direction algorithms for overland flow on general meshes, ESAIM: Mathematical Modelling and Numerical Analysis, Vol. 54 (6), pp. 1917-1949, 2020.

Davy, P. and Lague, D.: Fluvial erosion/transport equation of landscape evolution models revisited, Journal of Geophysical Research: Earth Surface, 114, https://doi.org/https://doi.org/10.1029/2008JF001146, 2009.

Desmet, P. J. J. and Govers, G.: Comparison of routing algorithms for digital elevation models and their implication for predicting ephemeral gullies, Int. J. Geo. Inf. Syst., Vol. 10(3), pp. 311-331, 1996.

DiPerna, R. and Lions, P.: Ordinary differential equations, transport theory and Sobolev spaces, Invent. Math. 98, 511-547, 1989.

Eymard, R., Gallouët, T., Gervais, V., and Masson, R.: Existence and uniqueness of a weak solution to a stratigraphic model, pp. 278–287, M. Feistauer, V. Dolejšì, P. Knobloch, K. Najzar (eds), Springer, Berlin, 2004.

Eymard, R., Gallouët, T., Gervais, V., and Masson, R.: Convergence of a numerical scheme for stratigraphic modeling, SIAM J. Numer. Anal., Vol. 43(2), pp. 474-501, 2005.

Fernández-Cara, E., Guillén, F., and Ortega, R.: Mathematical modeling and analysis of visco-elastic fluids of the Oldroyd kind, P.G. Ciarlet, J.L. Lions (Eds.), Numerical Methods for Fluids, Part 2, in: Handbook of Numerical Analysis, vol. VIII, North-Holland, Amsterdam, pp. 543–661, 2002.

Freeman, T. G.: Drainage with divergent flow over a regular grid, Proc. 8th Biennial Conf. Simulation Society of Australia, Canberra, pp. 160-165, 1989.

Freeman, T. G.: Calculating catchment area with divergent flow based on a regular grid, Computers & Geosciences Vol. 17(3), pp. 413-422, 1991.

Gallant, J. C. and Hutchinson, M. F.: A differential equation for specific catchment area, Water resources research, Vol. 47, W05535, 2011.

Gilbert, G.: Geology of the Henry Mountains, US Geographical and Geological Survey, Washington, D.C, 1880.

Girault, V. and Tartar, L.: L^p and $W^{1,p}$ regularity of the solution of a steady transport equation, C. R. Acad. Sci. Paris, Ser. I, Vol. 348, pp. 885-890, 2010.

Graf, W. H. and Altinakar, M. S.: Hydraulique fluviale: Ecoulement et phénomènes de transport dans les canaux à géométrie simple, Traité de génie civil, vol. 16, Presses polytechniques et universitaires romandes, 2000.

Granjeon, D.: Modélisation stratigraphique déterministe: Conception et applications d'un modèle diffusif 3-d multilithologique, Ph.D. thesis, Universit é de Rennes I, 1996.

Grospellier, G. and Lelandais, B.: The Arcane development framework, POOSC 09: Proceedings of the 8th workshop on Parallel/High-Performance Object-Oriented Scientific Computing, pp. 1–11, https://doi.org/https://doi.org/10.1145/1595655.1595659, 2009.

Guermond, J.-L., Oden, J., and Prudhomme, S.: An interpretation of the Navier-Stokes-alpha model as a frame-indifferent Leray regularization, Phys. D, Vol. 177(1-4), pp. 23-30, 2003.

Holmgren, P.: Multiple flow direction algorithms for runoff modelling in grid based elevation models: an empirical evaluation, Hydrological processes, Vol. 8, pp. 327-334, 1994.

Hooshyar, M. and Porporato, A.: Mean dynamics and elevation-contributing area covariance in landscape evolution models, Water Resources Research, Vol. 57, e2021WR029727, 2021a.

Hooshyar, M. and Porporato, A.: Spectral signature of landscape channelization, Geophysical Research Letters, Vol. 48, e2020GL091015, 2021b.

Hooshyar, M., S.Bonetti, Singh, A., Foufoula-Georgioui, E., and Porporato, A.: From turbulence to landscapes: Logarithmic mean profiles in bounded complex systems, Phys. Rev. E, 102, 033 107, 2020.

Leopold, L. B., Wolman, M. G., and Miller, J. P.: Fluvial Processes in Geomorphology, W. H. Freeman, San Francisco, California, 1964.

Leray, J.: Sur le mouvement d'un fluide visqueux emplissant l'espace, Acta Math., Vol. 63 pp. 193-248, 1934.

Maxwell, J. C.: On hills and dales, Philos. Mag. J. Sci., Vol. 4/40(269), pp. 421-427, 1870.

Pelletier, J.: 2.3 Fundamental Principles and Techniques of Landscape Evolution Modeling, in: Treatise on Geomorphology, edited by Shroder, J. F., pp. 29–43, Academic Press, San Diego, 2013.

Pelletier, J. D.: Minimizing the grid-resolution dependence of flow-routing algorithms for geomorphic applications, Geomorphology, Vol. 122 , pp. 91-98, 2010.

Perlin, K.: An image synthesizer, ACM SIGGRAPH Computer Graphics, 19, 287–296, https://doi.org/https://doi.org/10.1145/325165.325247, 1985.

Perron, J. T., Dietrich, W. E., and Kirchner, J. W.: Controls on the spacing of first-order valleys, J. Geophys. Res., Vol. 113, F04016, 2008.

Perron, J. T., Kirchner, J. W., and Dietrich, W. E.: Formation of evenly spaced ridges and valleys, Nature, Vol. 460, pp. 502-505, 2009.

Peton, N., Cancès, C., Granjeon, D., Tran, Q.-H., and Wolf, S.: Numerical scheme for a water flow-driven forward stratigraphic model, Computational Geosciences, vol. 24 pp. 37-60, 2020.

Porporato, A.: Hydrology without dimensions, Hydrol. Earth Syst. Sci., Vol. 26, pp. 355-374, 2022.

Scheingross, J. S., Limaye, A. B., McCoy, S. W., and Whittaker, A. C.: The shaping of erosional landscapes by internal dynamics, Nat Rev Earth Environ Vol. 1, pp. 661-676, 2020.

Smith, T. R. and Bretherton, F. P.: Stability and the Conservation of Mass in Drainage Basin Evolution, Water Resour. Res., Vol. 8(6), W03417, 1972.

Smith, T. R., Birnir, B., and Merchant, G. E.: Towards an elementary theory of drainage basin evolution: I The theoretical basis, Computers & Geosciences, Vol. 23(8), pp. 811-822, 1997.

Veiga, H. B. D.: Existence results in Sobolev spaces for a stationary transport equation, Ricerche Mat. Suppl. XXXVI pp. 173-184, 1987.

Zhiyin, Y.: Large-eddy simulation: Past, present and the future, Chinese Journal of Aeronautics, 28, 11–24, 2015.